University of Crete
Department of Physics

BACHELOR THESIS

The energy spectrum of accretion discs in AGN

Author:
Marios Papoutsis

Supervisor:
Iossif Papadakis

2022

Contents

Chapter 1: Introduction

1.1 What is an active galactic nucleus

An active galactic nucleus (AGN) is the central region of a galaxy where we observe energetic phenomena that cannot be attributed directly to stars. At least $\sim 10\%$ of galaxies in the near Universe host AGN. We list below the main observational properties of these active galactic nuclei.

1.2 AGN observational properties

In this subsection, we present the fundamental observational properties of AGN.

1) AGN show a bright star-like nucleus that, in some cases, can exceed the luminosity of the host galaxy. To be more specific, AGN luminosity ranges from $\sim 10^{42}$erg s^{-1} to $\sim 10^{47}$erg s^{-1}, while the luminosity of a typical galaxy is about $\sim 10^{44}$erg s^{-1}.

2) AGN show broadband emission at a wide range of frequencies. Figure (1) shows the spectral energy distribution (SED) of an AGN as a function of the frequency. As we can see, the spectrum extends from the radio frequencies (10^9Hz) all the way up to the $\gamma-$ray frequencies (10^{20}Hz). The SED of a normal galaxy is also shown for comparison. The normal galaxy emits at a significantly smaller part of the electromagnetic spectrum since its radiation originates mainly from stars. At the ultraviolet (UV) part of the spectrum ($10^{15} - 10^{16}$Hz), the emission of the normal galaxy falls off. On the other hand, the AGN emission increases with increasing frequency, in the UV band. This is a major difference between AGN and normal galaxies. This part of the AGN spectrum is known as the "big blue bump".

3) Figure (2) shows the mean spectrum created by averaging the spectra of over 700 AGN, in the optical and UV region. The strong increase of the emitted flux at short wavelengths can be seen clearly. Another important characteristic of AGN spectra is the presence of strong emission lines. These lines can be divided into two groups: the narrow lines, which have widths corresponding to velocities of several hundred kilometers per second, and the broad lines that have widths up to 10^4km s^{-1}.

4) A fraction of AGN ($\sim 10\%$ of their population) is characterized by strong radio emission. This is due to the synchrotron mechanism, and in some cases originates from two large, lobe-shaped regions. The lobes are located on either side of the galaxy center and are more or less symmetrical. Their extend can be as large as megaparsecs (1Mpc $= 10^6$pc, 1pc$=3.086 \times 10^{16}$m). The radio emission of such objects can be a million times stronger than the radio emission of a normal galaxy. Radio emission also originates from jet-like structures. The jets sizes range from astronomical units (AU) to megaparsecs and can produce radiation from radio waves to γ-rays in some cases. They seem to originate from the nucleus and have an outwards direction towards the radio lobes. The particles in these structures have bulk motions close to the speed of light.

5) Last but foremost, AGN are variable in every waveband they have been observed. The time-scale and the amplitude of the observed variations decrease and increase, respectively, with increasing frequency. Figure (3) shows the continuum and the emission-line light curves (left panels) of NGC 5548, which is a nearby AGN. The top two left panels show the ultraviolet and optical fluxes as a function of time. It is clear that they both change considerably with time. The bottom three panels show the variations of three broad emission lines. Interestingly, the pattern of these variations follows the variations of the continuum with a time delay. The right panels show the so-called cross-correlation function between the continuum variations at $\lambda = 1350$Å, and the continuum at 5100Å, and the 3 emission lines, whose light curves are plotted in the left panels. Cross-correlation is a statistical tool which is used to measure how well two light curves are correlated at various time

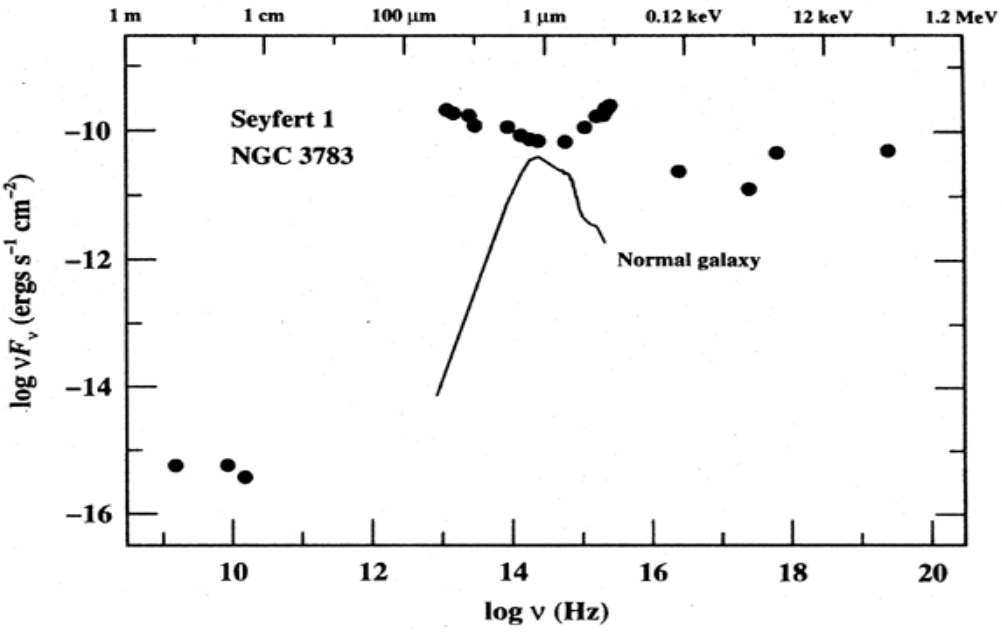

Figure 1: The spectral energy distribution (SED) of the AGN in NGC 3783 from radio to $\gamma-$ray frequencies as black dots. The solid line is the SED of a normal galaxy, (figure taken from Peterson, 1997).

scales. The amplitude of this function indicates how good the correlation is. The fact that the amplitude of the functions plotted in the right panel of Fig.(3) is close to 1 indicates that the light curves plotted in the left panel are indeed well correlated. In addition, the time-scale at which the maximum of the cross-correlation appears indicates the delay between the variations in the various energy bands.

1.3 AGN taxonomy

Active galactic nuclei can be divided into various types. The classification reflects their observational properties rather than the actual underlying physical differences between various classes, as we do not yet fully understand the physics of the AGN phenomenon.

AGN can be divided into radio-loud and radio-quiet sources, depending on whether we observe strong radio emission or not. The radio-quiet subclass includes Seyfert galaxies and quasars (also known as quasi-stellar objects QSOs). Seyfert galaxies exhibit strong, high-ionization emission lines and time-variable continuum emission in the infrared, optical, UV, and X-ray bands. Morphological studies suggest that Seyferts occur in spiral galaxies. They can be further divided into type 1 and type 2 Seyferts. Type 1 shows broad and narrow emission lines, while in type 2 only the narrow lines are present. The observational properties of quasars and Seyferts are similar with the former being more luminouns. Due to this property, quasars can be observed at great distances. A fraction of quasars can also be radio-loud sources that show emission from a jet.

The radio-loud subclass includes radio galaxies and Blazars. Radio galaxies are mainly hosted in elliptical galaxies and can be separated into broad-line radio galaxies and narrow-line radio galaxies as the radio-loud counterparts of Seyferts type 1 and type 2 respectively. Blazars include optically violent variables (OVVs), which are characterized by large flux variations and high polarization, and BL Lac objects, which share some of the OVVs properties and are distinguished by the absence

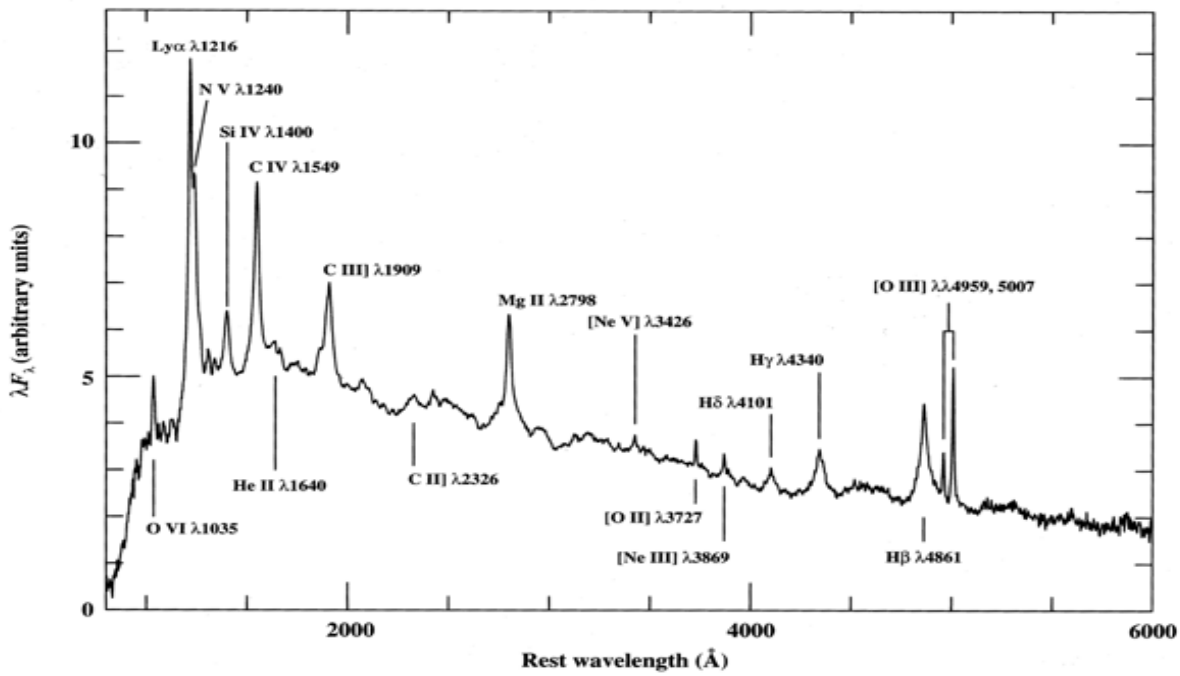

Figure 2: A mean AGN spectrum formed by averaging the spectra of over 700 AGN, at optical and ultraviolet wavelengths, (figure taken from Peterson, 1997).

of emission or absorption lines. The variability of Blazars is thought to originate from a strong relativistically beamed component which is oriented close to the line of sight.

Lastly, we note that there are efforts to unify the different models of AGN. These are based on the assumption that the observational characteristics of AGN are strongly dependent on the orientation of the system and that a single physical object can explain the observations when viewed from different angles.

1.4 The central "engine" of AGN

The AGN variability can help us estimate the size of the central nucleus. The top left panel of Fig.(3), shows that there is a noticeable change in the flux of the source (say by a factor of 2 or so) on a time-scale of ~ 25 days. Such a noticeable change must involve a significant variation in the properties of the source as a whole. This means that the nucleus cannot be larger than the variability time-scale multiplied by the maximum speed by which the information travels, i.e. the speed of light. Taking a typical time-scale of 25 days, $\Delta t \approx 20 \times 10^5$ sec, we can then set an upper limit to the size of the source as $R \leq c\Delta t = 6 \times 10^{16}$cm. This is of the order of ~ 0.02 pc.

A rough estimate of the nucleus mass can be made using the virial theorem. For a potential energy of the form $V \propto R^n$ the virial theorem takes the form $2 < K >= n < U >$. Considering a central mass M and gravitationally bound material of mass m at a distance R, we can write down the expressions for the kinetic and potential energy: $< K >= mv^2/2$, $< U >= -GMm/R$. Substituting $< K >$, $< U >$, and $n = -1$ in the virial equation, and solving for the mass M we find $M \approx v^2 R/G$. If the width of the emission lines observed in AGN spectra is due to Doppler broadening, then a typical value for the velocity is $v = 10^4$km s^{-1}. For the distance R we use the minimum size of the nucleus derived earlier, i.e. $R \sim 25$ light-days. This oversimplified analysis leads to a mass of $M \sim 5 \times 10^8 M_\odot$, where $M_\odot = 2 \times 10^{30}$kg is the mass of the sun. This means

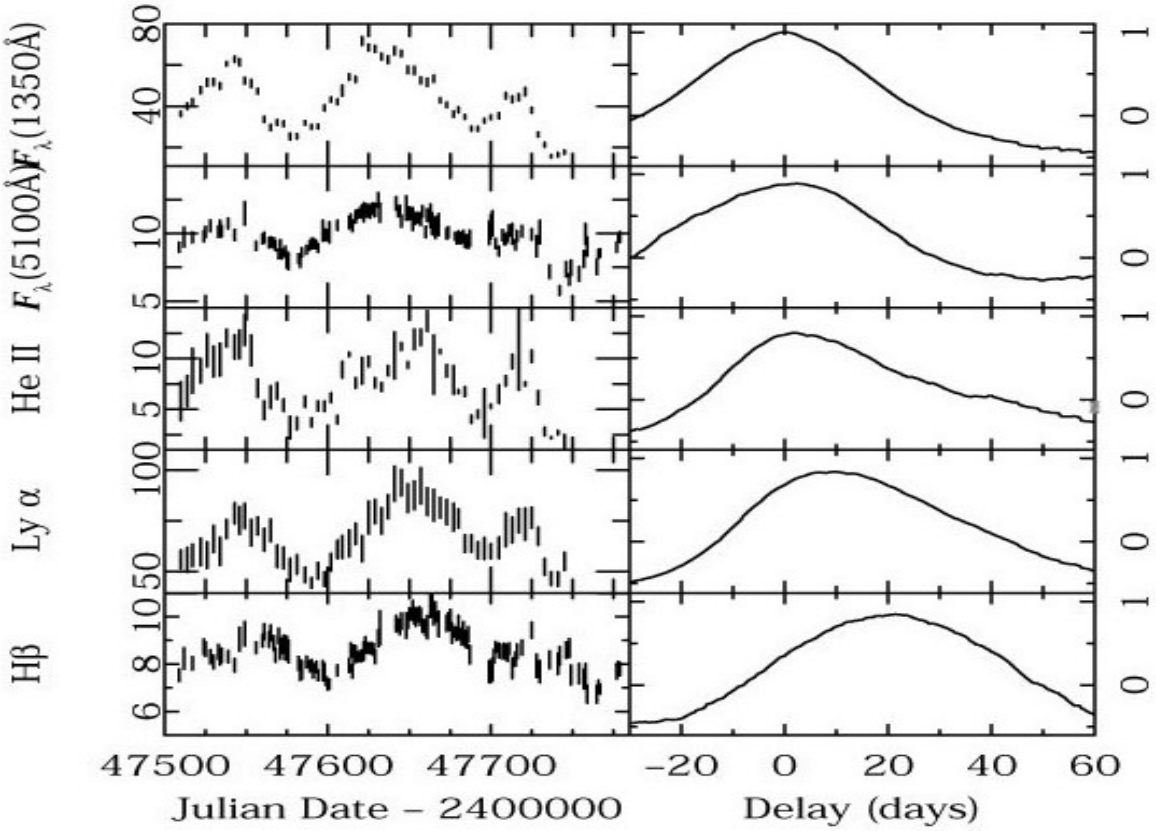

Figure 3: Light curves (left panels) and cross-correlation functions (right panels) for NGC 5548 (figure taken from Peterson, 1997).

that around a billion sun-like stars must lie in a region significantly smaller than 1pc to explain the mass of the AGN. Such a system would most likely be unstable. For this reason, a supermassive black hole (SMBH) is a more possible explanation. After all, the size of a black hole (BH) is given by the Schwarzschild radius $R_s = 2GM/c^2$, and for $M \sim 5 \times 10^8 M_\odot$, we find $R_s \sim 2 \times 10^{14}$cm, which is well below the parsec limit.

To fuel AGN we need an efficient energy production mechanism. If we assume a mass m travelling from infinity to a distance r from the central mass M, then the potential energy released is $U = GMm/r$. For a given mass M this energy increases as the small mass m reaches closer to the central mass, i.e. the distance r decreases. This distance r is minimized when the central object is a black hole. Assuming that the mass m travels up to the innermost stable circular orbit around the supermassive black hole, which is equal to $3R_s$, then the potential energy released is $U = GMm/(3R_s) = 0.17mc^2$. This means that approximately 17% of the mass is converted to energy. For reference, nuclear processes in stars have an efficiency of 0.7%. It turns out that the release of gravitational energy by infalling matter is the most efficient mechanism for converting mass to energy, and thus it can explain the large energy output that AGN show.

Based on the previous estimates for the size and the mass of an AGN, as well as the arguments on the energy production mechanism, it is reasonable to assume that the central engine of the AGN phenomenon is a supermassive black hole, surrounded by material that releases gravitational energy as it accretes into the black hole. As we discuss at the start of the next chapter, the material lies in an accretion disc that is heated to high temperatures. The aim of this work is to study the spectrum that the accretion discs around supermassive black holes emit.

Chapter 2: The structure and the emitted spectrum of the disc

2.1 Formation of the disc and the innermost stable circular orbit

Suppose a mass M, a supermassive black hole in our case, and gas particles spread out around it. The particles have random initial velocities and thus angular momentum. As a result, most of them cannot fall directly into the black hole. Instead, they follow circular trajectories, since that is the path of least energy around a spherically symmetric potential for a given angular momentum. These paths intersect, which leads to the collision of particles. The collisions tend to cancel the up and down motion of the gas which slowly accumulates to the plane perpendicular to the total angular momentum of the gas. The result is a disc where particles spin in circular orbits. However, for a non-rotating black hole the disc does not extend up to the event horizon. The innermost stable circular orbit (ISCO) is located at

$$R_{isco} = \frac{6GM}{c^2} = 3R_s, \tag{1}$$

where $R_s = 2GM/c^2$ is the Schwarzschild radius. This is because lowering the orbit beyond that point does not release enough potential energy to accelerate the particle to the speed necessary to maintain a stable circular orbit.

2.2 Viscosity

The basic assumption for the source of the enormous luminosity of AGN is accretion of matter to a supermassive black hole. As we mentioned above, gas in the disc is expected to rotate around the BH. If we assume Keplerian orbits, then

$$\Omega(R) = \sqrt{\frac{GM}{R^3}}\,, \tag{2}$$

where $\Omega(R)$ is the angular velocity at radius R, where R is the distance from the central mass, M. The circular velocity is then

$$\upsilon_\phi(R) = R\Omega(R)\,. \tag{3}$$

Equation (2) implies differential rotation, meaning that material in adjacent radii rotates with different angular velocities. In such conditions, internal friction between particles that are in relative motion arises. This resistance to the differential motion is known as viscosity. The work done by the shear stresses on the gas, due to viscosity, is dissipated to the disc as heat. The heat is then radiated away and thus the gas loses energy. However, the source of the gas energy is the gravitational potential. This means that viscosity turns gravitational potential energy into radiation. As a result, the gas moves closer to the black hole. This way, a negative radial velocity, υ_R, appears, and matter is accreted towards the BH.

In order to better demonstrate the role of viscosity, let us consider an annulus at radius R. Due to viscosity, there are torques acting on the annulus by the outer and inner disc parts. It turns out that the torque $\tau(R)$ exerted to the annulus at radius R, by the outer neighbouring annulus is given by the expression

$$\tau(R) = \underbrace{2\pi R}_{\text{circumference}} \cdot \underbrace{\nu\Sigma(R)R\frac{d\Omega}{dR}}_{\text{viscous force per unit length}} \cdot \underbrace{R}_{\text{lever}}\,, \tag{4}$$

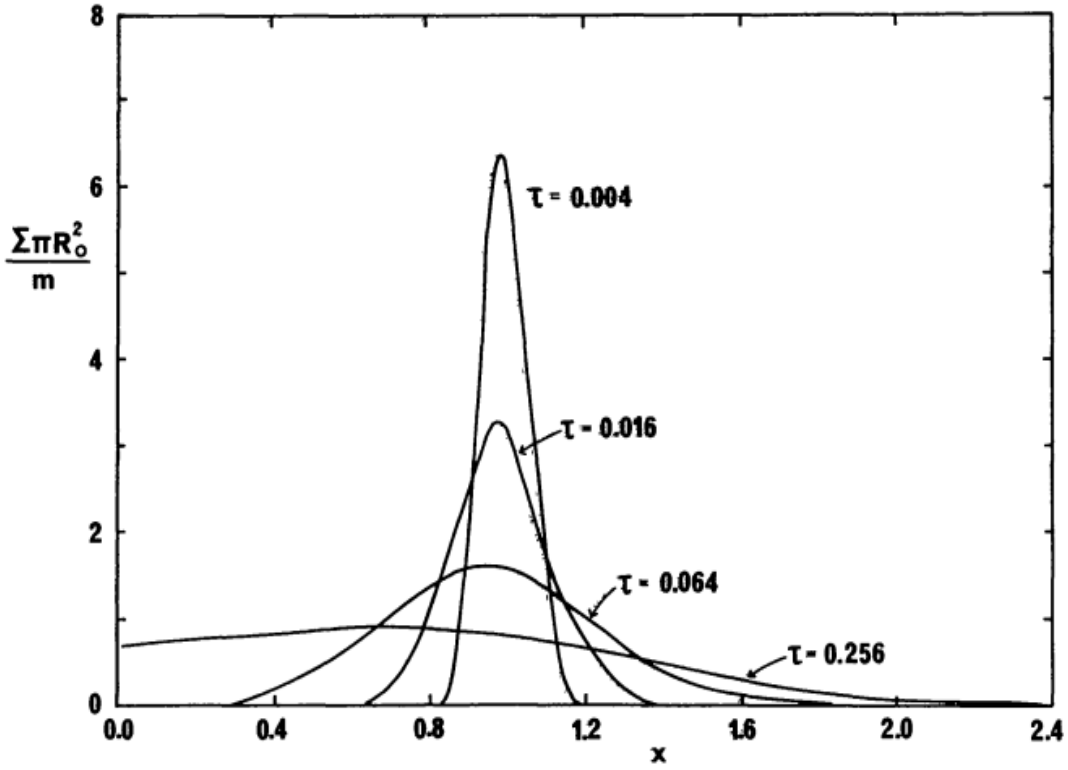

Figure 4: The surface density evolution for a ring of mass m at a distance R_0. The dimensionless parameters for the position and the time are $x = R/R_0$ and $\tau = 12\nu t R_0^{-2}$, where ν is the viscosity, (figure taken from Pringle, 1981).

where $\Sigma(R)$ is the surface density of the disc and the factor of proportionality ν is the kinematic viscosity. Equation (4) shows that, since $\Omega(R)$ decreases outwards, $\tau(R)$ is negative and thus the inner rings lose angular momentum to the outer ones. As a result, mass spirals closer to the black hole. This can also be seen by taking the expression for the specific angular momentum of the Keplerian disc (angular momentum per unit mass)

$$l = R^2\Omega(R) = \sqrt{GMR}\,. \tag{5}$$

This indicates that if a ring loses angular momentum it must move inward to remain in a Keplerian orbit (i.e. if l decreases then R must decrease as well).

Figure (4) shows the evolution of the surface density of a ring of mass m, which is originally located at radius $R = R_0$. We observe that as time passes, the mass in the initial ring spreads out to smaller and larger radii. Most of the matter is accreted inwards because it loses angular momentum due to viscosity. At the same time, angular momentum must be conserved, so a smaller amount of matter moves outwards to larger radii, carrying the angular momentum that the accreting matter lost.

2.3 Dissipation of energy by the viscous torques

Considering the ring of gas between R and $R + \Delta R$, shown in Figure (5), the net torque acting on it is

$$\tau(R + \Delta R) - \tau(R) = \frac{\partial \tau}{\partial R} dR\,, \tag{6}$$

where $\tau(R+\Delta R)$ is the torque exerted on the annulus by the outer ring, which slows down the annulus, while $\tau(R)$ is due to the inner ring, which speeds up the annulus. Multiplying eq.(6) by the angular velocity of the ring $\Omega(R)$ we get the rate of working by the torque

$$\Omega\frac{\partial\tau}{\partial R}dR = [\frac{\partial(\tau\Omega)}{\partial R} - \tau\Omega']dR\,, \tag{7}$$

where $\Omega' = d\Omega/dR$. If we integrate the term $[\partial(\tau\Omega)/\partial R]dR$ over the whole disc we get $[\tau\Omega]_{R_{inner}}^{R_{outer}}$. This implies that the term $\partial(\tau\Omega)/\partial R$ gives the work done by the torque determined at the edges of the disc. An expression for the local rate of work is given by the term $\tau\Omega' dR$. This work heats up the disc and will be, ultimately, radiated away. To calculate the power per unit surface area, $Q(R)$, that is provided by the torques, we divide $\tau\Omega' dR$ by the surface of the ring, keeping in mind that each ring has two plane faces, and thus a total area of $4\pi R dR$. We find that

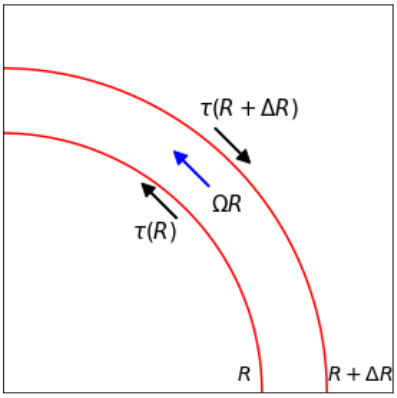

Figure 5: Viscous torques acting on an annulus of width ΔR.

$$Q(R) = \frac{\tau(R)\Omega'}{4\pi R}\,. \tag{8}$$

Then, we can substitute $\tau(R)$ from eq.(4) to get

$$Q(R) = \frac{1}{2}\nu\Sigma(R)(R\Omega')^2\,. \tag{9}$$

Our goal is to compute the energy spectrum emitted by the disc. To do so, it is important to compute $Q(R)$, since it holds the information for the power that the disc can radiate. Therefore, we need to know ν and $\Sigma(R)$. If the main mechanism behind viscosity is turbulence, then ν has the form of $\nu \sim h \cdot u$, where h is the size and u the speed of the largest eddies. Shakura & Sunyaev (1973) introduced the dimensionless parameter α and wrote ν as

$$\nu = \alpha c_s H\ , \tag{10}$$

where c_s is the sound speed, H is the disc thickness and $a \leq 1$. This parametrization allows us to study accretion discs efficiently, without complete knowledge of the underlying mechanism behind viscosity. We note that ν can be a function of R for discs of non-constant H or c_s. In the next section, we discuss the disc surface density, $\Sigma(R)$.

2.4 Radial disc structure

We use the conservation of mass and angular momentum to derive an expression for the surface density $\Sigma(R)$ of the disc, i.e. mass per unit surface. We consider the case of a constant accretion rate, which means that the disc is characterized by a steady-state structure and the disc parameters do not vary with time, i.e. $\partial/\partial t = 0$ in all equations.

2.4.1 Conservation of mass

Let us consider an annulus of gas with inner radius R and outer radius $R+\Delta R$, as in Fig.(5). The mass of the annulus is $2\pi R \cdot \Delta R \cdot \Sigma(R)$. Since matter is accreted towards the central compact

object, the rate of change of the mass in the annulus is equal to the flow of matter from neighboring annuli

$$\frac{\partial}{\partial t}(2\pi R\cdot\Delta R\cdot\Sigma)=\upsilon_R(R,t)\cdot 2\pi R\cdot\Sigma(R,t)-\upsilon_R(R+\Delta R,t)\cdot 2\pi(R+\Delta R)\cdot\Sigma(R+\Delta R,t)\,. \quad (11)$$

The first term on the right hand side of the equation is the mass that leaves the annulus, while the the second term is the mass that is being added to the annulus. Note that the radial velocity υ_R is negative, since matter moves inward. We divide both terms by ΔR and then take the limit $\Delta R\to 0$ to get,

$$\frac{\partial}{\partial t}(R\Sigma)=-lim_{\Delta R\to 0}\frac{\upsilon_R(R+\Delta R,t)\cdot(R+\Delta R)\cdot\Sigma(R+\Delta R,t)-\upsilon_R(R,t)\cdot R\cdot\Sigma(R,t)}{\Delta R}\Rightarrow \quad (12)$$

$$R\frac{\partial\Sigma(R)}{\partial t}+\frac{\partial}{\partial R}[R\Sigma(R)\upsilon_R(R)]=0\,. \quad (13)$$

This is the equation of mass continuity. Using the steady-state assumption eq.(13) becomes

$$\frac{\partial}{\partial R}[R\Sigma(R)\upsilon_R(R)]=0\Rightarrow R\Sigma(R)\upsilon_R(R)=constant\,. \quad (14)$$

We note that since $M(R)=2\pi R\Delta R\Sigma(R)$, then the accretion rate at R is given by

$$\dot{M}=2\pi R\frac{\Delta R}{\Delta t}\Sigma\Rightarrow\dot{M}=-2\pi R\upsilon_R(R)\Sigma(R)\,. \quad (15)$$

The minus sign accounts for the fact that $\dot{M}$ is positive when υ_R is negative. Conservation of mass, i.e. eq.(14), implies that $\dot{M}$ is the same at all radii.

2.4.2 Conservation of angular momentum

The angular momentum of the same annulus is $2\pi R\cdot\Delta R\cdot\Sigma(R)\cdot R^2\Omega(R)$. Due to the flow of matter and the fact that matter carries angular momentum, we have flow of angular momentum as well. Therefore, the change in the angular momentum of the annulus is caused by the flow of angular momentum from neighboring annuli, and the viscous torques $\tau(R)$, from the adjacent annuli

$$\frac{\partial}{\partial t}(2\pi R\cdot\Delta R\cdot\Sigma\cdot R^2\Omega)=\upsilon_R(R,t)\cdot 2\pi R\cdot\Sigma(R,t)\cdot R^2\Omega(R)$$

$$-\upsilon_R(R+\Delta R,t)\cdot 2\pi(R+\Delta R)\cdot\Sigma(R+\Delta R,t)\cdot(R+\Delta R)^2\Omega(R+\Delta R)+\tau(R+\Delta R)-\tau(R)\,. \quad (16)$$

The first term of the right hand side equals the angular momentum that is carried away from the annulus, while the second term is the angular momentum that flows into the annulus. The term $\tau(R+\Delta R)$ is the torque from the outer ring, and $\tau(R)$ is the torque from the inner ring. Dividing by ΔR and taking the limit for small ΔR like before we have

$$R\frac{\partial}{\partial t}(\Sigma R^2\Omega)+\frac{\partial}{\partial R}(R\Sigma\upsilon_R R^2\Omega)=\frac{1}{2\pi}\frac{\partial\tau}{\partial R}\,. \quad (17)$$

Using the steady disc assumption eq.(17) becomes

$$\frac{\partial}{\partial R}(R\Sigma\upsilon_R R^2\Omega)=\frac{1}{2\pi}\frac{\partial\tau}{\partial R}\,. \quad (18)$$

Let us integrate the equation above,

$$\int \frac{\partial}{\partial R}(R\Sigma v_R R^2\Omega)dR = \frac{1}{2\pi}\int \frac{\partial \tau}{\partial R}dR + \frac{C}{2\pi} \Rightarrow \tag{19}$$

$$R^3\Sigma(R)v_R(R)\Omega(R) = \frac{\tau}{2\pi} + \frac{C}{2\pi} \tag{20}$$

We use eq.(4) to substitute τ in the above equation. We find

$$R^3\Sigma(R)v_R(R)\Omega(R) = \nu\Sigma(R)R^3\frac{d\Omega(R)}{dR} + \frac{C}{2\pi} \Rightarrow \tag{21}$$

$$\nu\Sigma(R)\frac{d\Omega(R)}{dR} = \Sigma(R)v_R(R)\Omega(R) + \frac{C}{2\pi R^3}\,. \tag{22}$$

To evaluate the constant C we can use the fact that at the inner edge of the disc, R_{isco}, the gradient of the angular velocity vanishes, i.e. $d\Omega/dR = 0$. This yields:

$$0 = \Sigma(R_{isco})v_R(R_{isco})\Omega(R_{isco}) + \frac{C}{2\pi(R_{isco})^3} \Rightarrow$$

$$C = -2\pi R_{isco}\cdot\Sigma(R_{isco})\cdot v_R(R_{isco})\cdot(R_{isco})^2\cdot\Omega(R_{isco})\,. \tag{23}$$

We can simplify this by using the relation for the accretion flow $\dot{M}$ given in (15). Setting $R = R_{isco}$ in eq.(15) and substituting in the expression for C we get

$$C = \dot{M}\cdot(R_{isco})^2\cdot\Omega(R_{isco})\,. \tag{24}$$

We can use the formula for the angular velocity of a circular Keplerian orbit from eq.(2), to get

$$C = \dot{M}\sqrt{GMR_{isco}}\,. \tag{25}$$

We substitute C in (22) and take the derivative $(d\Omega/dR) = -(3/2)\sqrt{GM/R^5}$ to find

$$-\frac{3}{2}\nu\Sigma(R)\sqrt{\frac{GM}{R^5}} = \Sigma(R)v_R(R)\sqrt{\frac{GM}{R^3}} + \frac{\dot{M}\sqrt{GMR_{isco}}}{2\pi R^3} \Rightarrow$$

$$\Sigma(R) = -\frac{2}{3\nu}\Sigma(R)v_R(R)R - \frac{1}{3\pi\nu}\dot{M}\sqrt{\frac{R_{isco}}{R}}\,. \tag{26}$$

We notice from (15) that $\Sigma(R)v_R(R)R = -\dot{M}/(2\pi)$. Also, we can replace R_{isco} with $3R_s$ since that is the innermost stable circular orbit, in the case of a non-rotating black hole. We thus reach to the following expression for the surface density of the disc

$$\Sigma(R) = \frac{\dot{M}}{3\pi\nu}\Big(1 - \sqrt{\frac{3R_s}{R}}\Big)\,. \tag{27}$$

2.5 Dissipation of energy by the viscous torques-Revisited

Now, we can use eq.(27) to substitute $\Sigma(R)$ in eq.(9) and take the derivative of $\Omega(R)$ to find

$$Q(R) = \frac{3}{8\pi}\frac{GM\dot{M}}{R^3}\Big(1 - \sqrt{\frac{3R_s}{R}}\Big)\,. \tag{28}$$

This is a significant result since $Q(R)$ turns out to be independent of the kinematic viscosity ν. This result means that despite our ignorance of the physical nature of viscosity we can calculate the required quantities for the computation of the disc spectrum. This will be the case, as long as ν can be adjusted to provide the steady mass flux $\dot{M}$, that is necessary to heat the disc.

2.6 The disc energy spectrum

We can compute the energy spectrum of the accretion disc, assuming that each disc annulus radiates as a black body. The blackbody emitted power per unit area is given by the Stefan–Boltzmann law

$$j(R) = \sigma T^4(R) \text{ (erg s}^{-1} \text{ cm}^{-2}) \,, \tag{29}$$

where σ is the Stefan–Boltzmann constant and $T(R)$ the temperature at radius R. We can find an analytic formula for this temperature by equating $j(R)$ to the dissipation rate $Q(R)$ given by (28), as follows:

$$\sigma T^4(R) = \frac{3}{8\pi}\frac{GM\dot{M}}{R^3}\Big(1 - \sqrt{\frac{3R_s}{R}}\Big) \Rightarrow \tag{30}$$

$$T(R) = \Big[\frac{3GM\dot{M}}{8\pi R^3\sigma}\Big(1 - \sqrt{\frac{3R_s}{R}}\Big)\Big]^{1/4}. \tag{31}$$

Knowing $T(R)$, the specific intensity of each annulus of the disc will be given by the Planck function

$$B_\nu[T(R)] = \frac{2h\nu^3}{c^2}\frac{1}{e^{h\nu/kT(R)} - 1} (\text{erg s}^{-1} \text{ cm}^{-2} \text{ Hz}^{-1} \text{ sr}^{-1}). \tag{32}$$

Let us assume that the disc is located at a distance D from an observer at O, as shown in Fig.(6). Then the specific radiative flux (also called net flux) of the whole disc at frequency ν is obtained by integrating over all solid angles subtained by the observer at O, i.e.

$$F(\nu) = \int B_\nu \cos\theta d\Omega \text{ (erg s}^{-1} \text{ cm}^{-2} \text{ Hz}^{-1}) \,. \tag{33}$$

Substituting the differential solid angle in spherical coordinates $d\Omega = \sin\theta d\theta d\phi$ and integrating over $d\phi$ we get

$$F(\nu) = 2\pi \int_{\theta_1}^{\theta_2} B_\nu \cos\theta \sin\theta d\theta \,, \tag{34}$$

where θ_1, θ_2 are illustrated in Figure (6). We can make the change of variables $\theta \to R$ using

$$\tan\theta = \frac{R}{D} \Rightarrow d\theta = \cos^2\theta \frac{dR}{D}, \; \sin\theta = \frac{R}{\sqrt{R^2 + D^2}}, \; \cos\theta = \frac{D}{\sqrt{R^2 + D^2}}. \tag{35}$$

Then the integral becomes

$$F(\nu) = \frac{2\pi}{D^2} \int_{R_{inner}}^{R_{outer}} B_\nu[T(R)] R dR \,, \tag{36}$$

where R_{inner} and R_{outer} are the boundaries of the disc. We also used the approximation $R^2 + D^2 \approx D^2$. Lastly, if ξ is the angle between the line of sight of the observer at O and the normal to the disc plane, then we should multiply eq.(36) by a factor of $\cos\xi$. We also use eq.(32) to end up with

$$F(\nu) = \frac{4\pi h\nu^3 \cos\xi}{c^2 D^2} \int_{R_{inner}}^{R_{outer}} \frac{R dR}{e^{h\nu/kT(R)} - 1} \,. \tag{37}$$

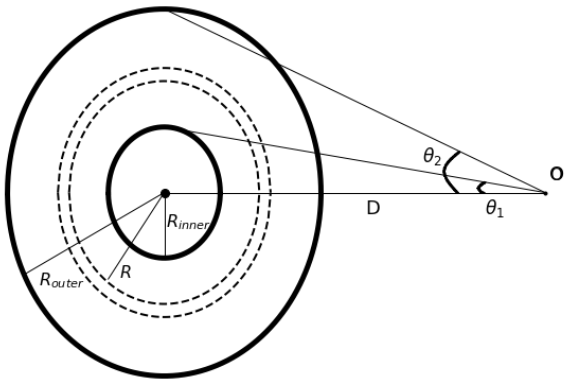

Figure 6: Disc illustration.

2.7 Computation of the disc spectrum

Using equation (31) we can compute the disc temperature at any radius, and with equation (37) we can calculate the flux of the disc at any frequency, ν. We thus have all the information we need to compute the disc energy spectrum. To do so, we divide the disc into small annuli, and we consider a range of frequencies at which we will compute $F(\nu)$, by numerically calculating the integral of eq.(37). Ideally, we would divide the disc into infinitely narrow annuli so that the computation of the integral is accurate. However, the runtime of the script to compute the disc energy spectrum should also be reasonable. With that in mind, we will figure out the optimal way to break up the disc into rings by studying its temperature profile.

2.7.1 The temperature profile

The temperature of each disc annulus is calculated by eq.(31). To make this calculation simpler we introduce the dimensionless parameters

$$r \equiv \frac{R}{R_s},\ \dot{m} \equiv \frac{\eta \dot{M} c^2}{L_{Edd}}\ , \tag{38}$$

where $\eta = 0.057$ is the efficiency of accretion into a non-rotating black hole, and L_{Edd} is the Eddington luminosity given by

$$L_{Edd} = \frac{4\pi G M m_p c}{\sigma_T}\ , \tag{39}$$

with m_p being the proton mass and σ_T the Thomson scatteting cross section. Then, using eq.(38), equation (31) becomes

$$T(r) = \Big[\frac{3}{8}\frac{c^3 m_p}{\eta \sigma_T \sigma}\frac{1}{R_s}\frac{\dot{m}}{r^3}(1-\sqrt{\frac{3}{r}})\Big]^{1/4}\ . \tag{40}$$

Figure (7) shows a plot of the temperature versus the dimensionless radius r, for $M = 10^7 M_\odot$, and $\dot{m} = 0.05$. Both axes on this plot are in logarithmic scale. The disc temperature in Fig.(7) is calculated at $N_r = 200$ radii, which are equidistant in the log space, i.e.

$$\log(r_i) = \log(r_{in}) + i\frac{[\log(r_{out}) - \log(r_{in})]}{N_r} \tag{41}$$

where $r_{in} = 3$ and $r_{out} = 5000$.

The temperature at $r = r_{in}$ is zero, since we have assumed that the torque vanishes at r_{isco}. Fig.(7) shows that, initially the temperature increases quickly and reaches a maximum at

$$\frac{dT}{dr} = 0 \Rightarrow \Big[\frac{3}{8}\frac{c^3 m_p}{\eta\sigma_T\sigma}\frac{\dot{m}}{R_s}\Big]^{1/4}\frac{d}{dr}\Big[\frac{1}{r^{3/4}}(1-\sqrt{\frac{3}{r}})^{1/4}\Big] = 0 \Rightarrow$$

$$-\frac{3}{4}\frac{1}{r^{7/4}}(1-\sqrt{\frac{3}{r}})^{1/4} + \frac{1}{r^{3/4}}\frac{1}{4}(1-\sqrt{\frac{3}{r}})^{-3/4}(\frac{\sqrt{3}}{2}\frac{1}{r^{3/2}}) = 0 \Rightarrow$$

$$-2\sqrt{r}(1-\sqrt{\frac{3}{r}}) + \frac{\sqrt{3}}{2} = 0 \Rightarrow r = \frac{49}{36}3 = 4.08\ . \tag{42}$$

The temperature at $r = 4.08$ equals $T_{max} = 1.292 \times 10^5$K, for our case of $M, \dot{m}$. At larger radii, the temperature decreases as $T(r) \propto r^{-3/4}$, because as we move to the outer parts of the disc $Q(R)$ decreases as well. This is expected since the gravitational energy released from matter far away

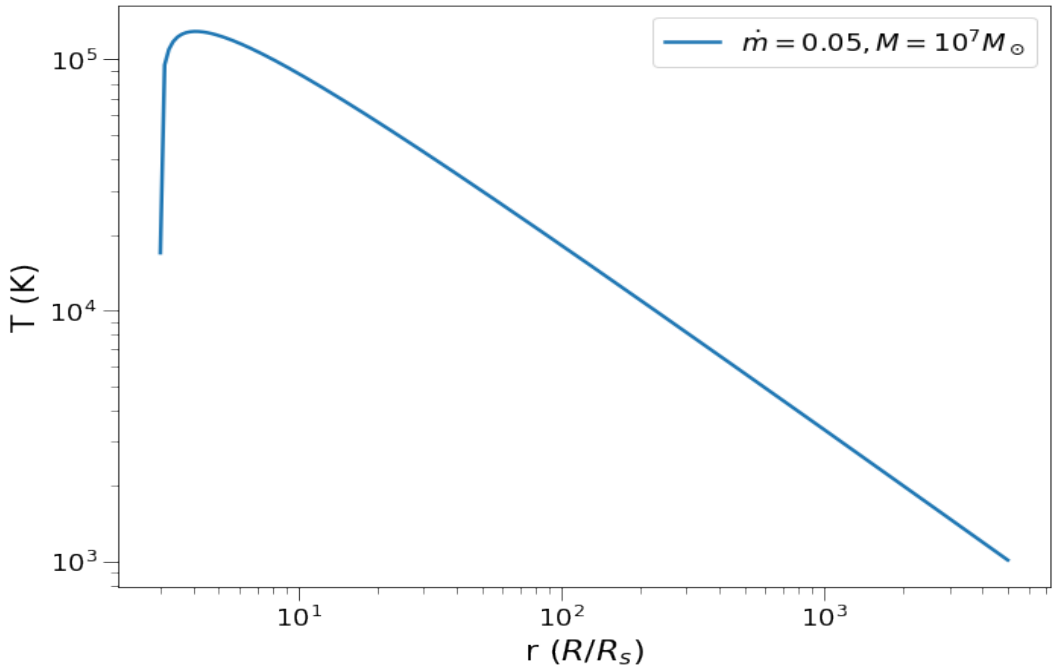

Figure 7: The disc temperature radial profile ($M = 10^7 M_\odot$, and $\dot{m} = 0.05$).

from the center is small compared to that of matter accreting close to the black hole. To get a better understanding of this effect, let us consider the gravitational potential around a mass M given by $V = -GM/R$ (erg/g). The change in the potential energy of a unit mass particle as it moves from $1100R_s$ to $1000R_s$ will be $\Delta V_1 = GM/11000R_s$. The potential energy released by the same particle as it moves from $200R_s$ to $100R_s$ will be $\Delta V_2 = GM/200R_s$, which is 55 times larger. Thus, more energy per mass is released in the central regions of the disc, hence the disc will be significantly hotter in the inner parts.

Equation (40) shows that the disc temperature increases with increasing $\dot{m}$. This is because, the rate of the gravitational power that is released, at each radius, depends on the rate of the mass that is accreted, i.e. $\dot{V} = -G\dot{M}/R$. We also note that $T(r)$ is inversely proportional to R_s, i.e. the black hole mass. Larger BH masses, will imply lower temperatures at all radii, for the same accretion rate. To understand this, let us consider the potential change $\Delta V_2 = GM/200R_s$ that we calculated before. Substituting $R_s = 2GM/c^2$ we find $\Delta V_2 = c^2/400$, which means that the potential energy released by a unit mass travelling from $200R_s$ to $100R_s$ is the same for all BH masses. However, the distance travelled, i.e. $100R_s$, is longer for a heavier BH. This means that the same amount of energy is dissipated to a larger area, and thus the disc temperature is lower for heavier masses.

Figure (7) shows that the curvature of the temperature profile is very steep at small radii. To investigate this issue, we calculate the percentage difference of the temperature at successive radii as follows:

$$\frac{|\Delta T|}{T} = \frac{|T(r_{i+1}) - T(r_i)|}{T(r_{i+1})} 100\% \,, \tag{43}$$

where r_i, r_{i+1} are the disc radii defined by eq.(41). This way eq.(43) represents the percentage change in temperature between the outer radius, r_{i+1}, and the inner radius, r_i, of each disc annulus. Figure (8) shows a plot of $|\Delta T|/T$ as a function of the radius (orange points), up to $r = 50$. The temperature between the inner and outer border of the innermost annuli may change by a factor of $5-85\%$. This implies that the numerical calculation of the integral in (37) is prone to large round-off

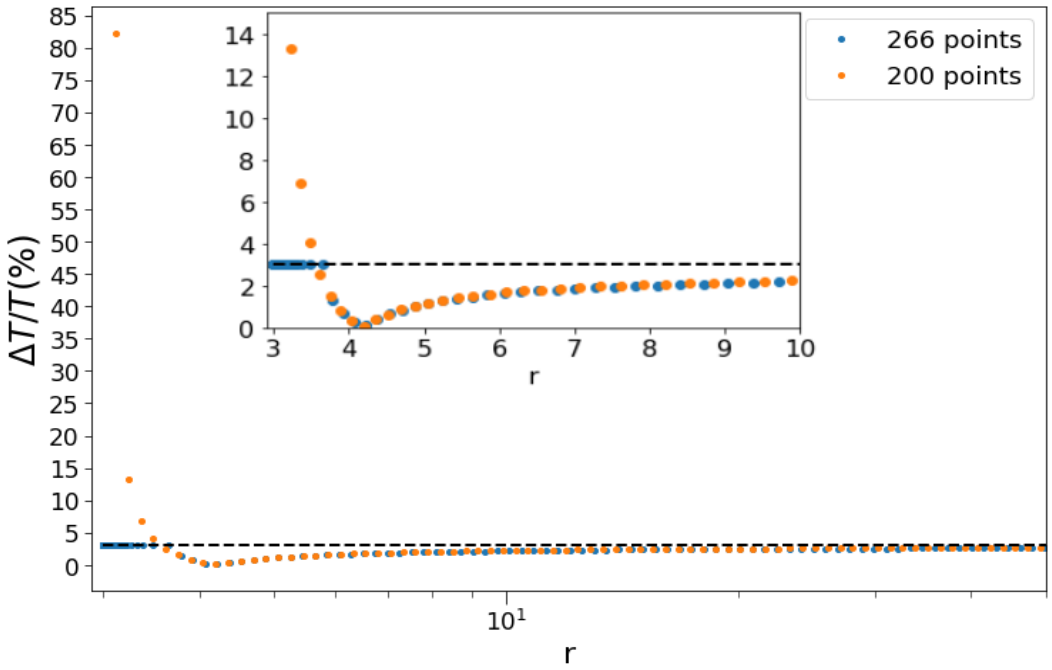

Figure 8: Percentage difference of temperature between outer and inner radii of the disc annuli below $r = 50$ (and below $r = 10$ in the embedded plot). The horizontal line in both plots indicates the 3% limit.

errors, due to the large temperature gradient of the innermost rings. On the other hand, the disc annuli at radii around the temperature peak appear well approximated by a constant temperature, as $|\Delta T|/T$ is smaller than $1 - 2\%$ in this case. At larger radii, the temperature difference increases slowly with radius and reaches a value of $\sim 3\%$ at $r \sim 50$, which remains constant at larger radii. To account for the large temperature variations in the inner disc, we divided the part below $r = 4$ to more annuli so that the temperature difference between r_{i+1} and r_i is fixed at 3%. This is done by solving numerically the equation

$$\frac{|\Delta T|}{T} = \frac{|T(r_{i+1}) - T(r_i)|}{T(r_{i+1})} = 0.03 \, , \tag{44}$$

where $T(r)$ is given by eq.(40). We start with $r_1 = r_{isco}$ and we compute r_2 by solving eq.(44). Then we proceed to the next annulus, where we compute r_3 using the previously calulated r_2, and so on until we reach $r_{i+1} > 4$. Then we divide the remaining disc in 200 rings, using eq.(41). We end up with a disc consisting of 265 annuli. Blue points in Figure (8) show $|\Delta T|/T$ for the new annuli. The differences are indeed fixed at 3%(dashed line) at $r < 4$, while at larger radii they are smaller than 3%.

2.7.2 The disc spectrum

The energy spectrum of the disc is computed by eq.(37). Using dimensionless parameters, eq.(37) becomes,

$$F(\nu) = \frac{4\pi h\nu^3 R_s^2 \cos\xi}{c^2 D^2} \int_{r_{in}}^{r_{out}} \frac{r dr}{e^{h\nu/kT(r)} - 1} \, . \tag{45}$$

We computed $F(\nu)$ at $N_\nu = 500$ frequencies, which are equidistant in log space, i.e.

$$\log(\nu_i) = \log(\nu_{low}) + i\frac{\log(\nu_{high}) - \log(\nu_{low})}{N_\nu} \ , \tag{46}$$

where $\nu_{low} = 10^{13} Hz$ ($\lambda = 30\mu m$; this is a wavelength in the infrared part of the spectrum), and $\nu_{high} = 3 \times 10^{16} Hz$ ($\lambda = 100$Å; this is a wavelength in the ultraviolet part of the spectrum). At each frequency ν_i we solved the integral in eq.(45) numerically using the trapeziodal rule. Therefore, integral (45) becomes

$$F(\nu_i) \approx \frac{4\pi h\nu_i^3 R_s^2 \cos\xi}{c^2 D^2} \sum_{j=0}^{N} \frac{1}{2}\left(\frac{r_j}{e^{h\nu_i/kT_j} - 1} + \frac{r_{j+1}}{e^{h\nu_i/kT_{j+1}} - 1}\right)\Delta r_j \ , \tag{47}$$

where $N = 264$ (since we start counting from $j = 0$), r_j and r_{j+1} are the inner and outer radius of the previously defined 265 rings and $\Delta r_j = r_{j+1} - r_j$.

In Figure (9) we present the spectrum for the case of $\dot{m} = 0.05$, $M = 10^7 M_\odot$, for an accretion disc at a distance $D = 1\text{Mpc} = 3.086 \times 10^{24}$cm and inclination and $\xi = 0^o$ (i.e. face on). The spectrum we observe in Fig.(9) is the result of the superposition of all the annuli spectra. The vertical dashed lines indicate the frequencies at which the black body emission from the outer annulus and the annulus with the highest temperature peak. At frequencies lower than $\nu_1 = 6 \times 10^{13}$Hz, the spectrum increases approximately as $F(\nu) \propto \nu^2$. This is because that part of the spectrum is equal to the sum of the Rayleigh-Jeans emission, i.e. $2kT\nu^2/c^2$, of all the annuli spectra. At frequencies higher than $\nu_2 = 7.6 \times 10^{15}$Hz, the spectrum falls off as $F(\nu) \propto \nu^3 e^{-h\nu/kT}$. The main contribution to the spectrum here is the Wien part of the ring with the highest temperature. At frequencies between ν_1 and ν_2, the spectrum slightly increases as $F(\nu) \propto \nu^{1/3}$, up to the frequency $\nu_{peak} = 2.2 \times 10^{15}$Hz where it reaches a maximum. We also notice that ν_{peak} is smaller than ν_2. This means that although the innermost rings with the highest temperatures have not yet reached their maximum, the spectrum has already started to fall off. This happens because the radiation of each annulus depends on its area as well and the area of the innermost rings is small.

In Figure (10), we have plotted the spectrum in units of erg/sec/cm^2, i.e. we show the emitted disc power as a function of the frequency. To compute this we simply multiply each point of Fig.(9) by its respective frequency. Figure (10) shows where most of the power is emitted. In our case, this is at a frequency of $\nu_{peak} = 6.7 \times 10^{15} Hz$, which corresponds to a wavelength of $\lambda_{peak} = 450$Å. In other words, for a BH mass of $M = 10^7 M_\odot$, which accretes at a rate of $\dot{m} = 0.05$, most of the radiated power is released in the UV part of the spectrum. This is consistent with the observations of the "big blue bump" in AGN spectra. Note that the maximum of Fig.(10) does not change when we convert frequencies to wavelengths since at the maximum we know that $\nu_{peak} F(\nu_{peak}) = \lambda_{peak} F(\lambda_{peak})$ and for this reason we can calculate λ_{peak} from $\lambda_{peak} = c/\nu_{peak}$. This is not the case for the maximum of Fig.(9).

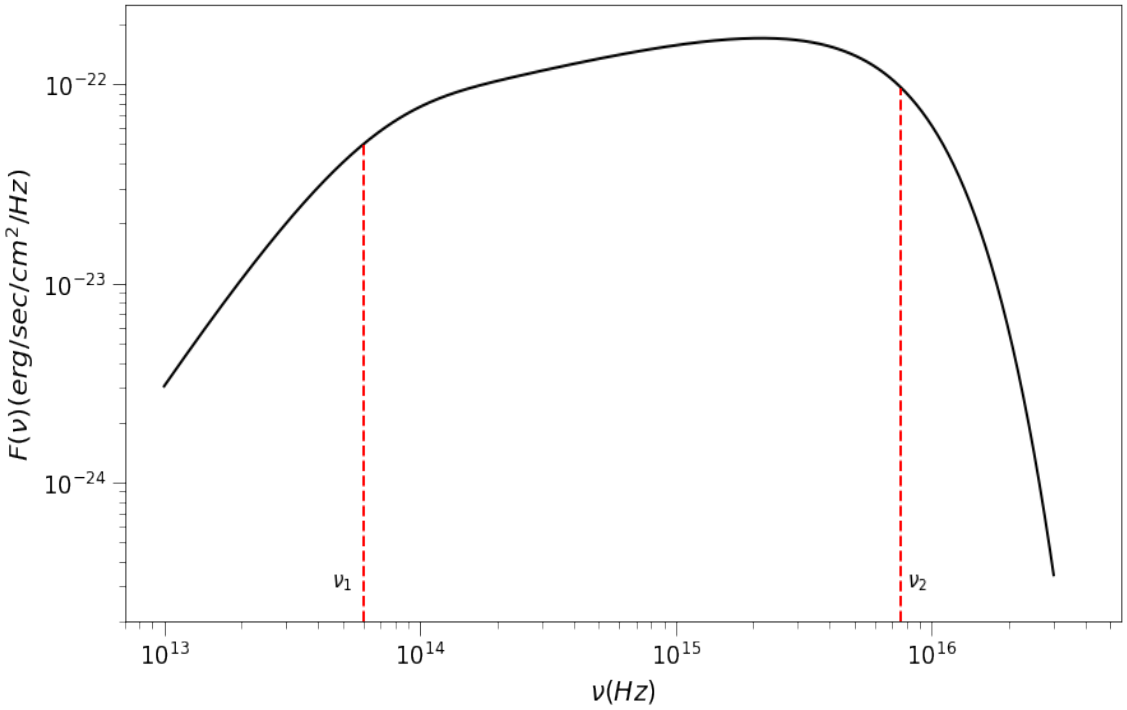

Figure 9: Energy spectrum of an accretion disc with accretion rate $\dot{m} = 0.05$, around a central black hole of mass $M = 10^7 M_\odot$, at a distance of $D = 1$Mpc, and inclination $\xi = 0$.

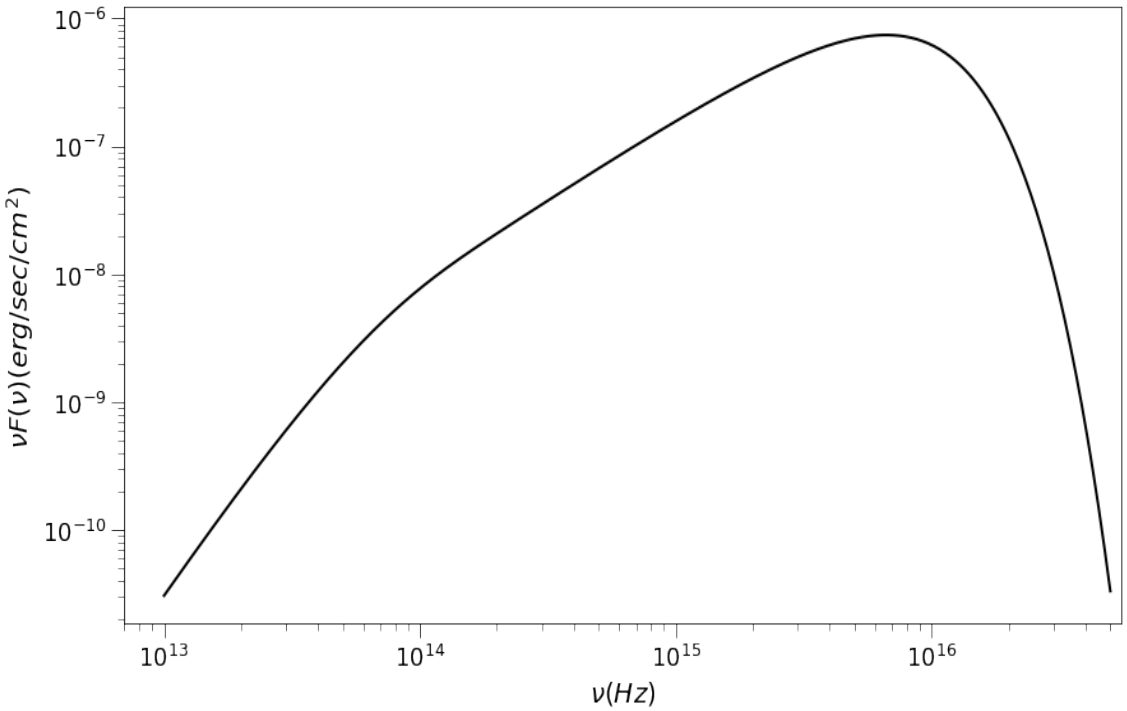

Figure 10: Same as in Fig.(9) but in units of $\nu F(\nu)$ (i.e. erg/sec/cm^2).

Chapter 3: The "modified" black body disc energy spectrum

3.1 The "modified" spectrum of the disc

In reality, disc spectra are more complicated than just the sum of black body spectra at the temperature given by eq.(31). This is because the black body is an idealization of a body that can absorb all the incident radiation and is at thermodynamic equilibrium with its environment, meaning that it emits as much radiation as it absorbs and has a constant temperature. This is not the case for physical objects like stars and accretion discs, since they are not in thermal equilibrium with the space around them. Clearly, the disc temperature and density vary along the vertical direction z. Therefore, to compute the emergent spectrum we need to perform radiative transfer through the vertical structure at each radius, considering all the interactions between photons and matter, such as bound-free and free-free absorption, Thomson and Compton scattering.

A way to include some of these opacity effects while not having to deal with the full radiative transfer is to consider the radiative flux of the disc at each frequency to be that of a modified black body, given by (Rybicki & Lightman, 1979)

$$I_\nu = \frac{4h\nu^3/c^2}{(e^{h\nu/kT_s}-1)(1+\sqrt{1+\kappa_\tau/\kappa_{ff}})}(\text{erg s}^{-1}\ \text{cm}^{-2}\ \text{Hz}^{-1}\ \text{ster}^{-1})\ , \tag{48}$$

where T_s is the disc surface temperature, and κ_T, κ_{ff} are the opacities for Thomson scattering and free-free absorption, respectively. Equation (48) is valid for a medium in which scattering, absorption, and emission occur. It assumes that the medium is homogeneous and isothermal. This is a good approximation for each annulus of a thin disc because we take their width to be small. It further assumes that scattering is isotropic. In the case of an accretion disc where Thomson scattering dominates, this assumption is valid. Equation (48) also ignores bound-free opacity. This is a reasonable approximation since at high temperatures, such as those in the innermost parts of the disc, the matter, which is mostly made up of hydrogen and helium, is fully ionized and thus there are only free-free transitions. To be more specific, fully ionized hydrogen is expected for temperatures around $10000K$. Figure (7) shows that in the case when $M = 10^7 M_\odot$ and $\dot{m} = 0.05$, $T \leq 10000$K at radii larger than $200R_s$. At larger radii, the temperature can be low enough for bound-free and bound-bound transitions to be present, however we will not consider the opacity effects due to those effects.

In the cases where Thomson scattering is negligible compared with free-free absorption, I_ν approaches the spectrum of a black body, B_ν. On the other hand, when $\kappa_T \gg \kappa_{ff}$ the spectrum becomes that of a modified black body, i.e. $I_\nu = 2B_\nu\sqrt{\kappa_{ff}/\kappa_T}$. The opacities are given by,

$$\kappa_T = \frac{\sigma_T}{m_p} = 0.4\ (\text{cm}^2\ \text{g}^{-1}) \tag{49}$$

$$\kappa_{ff} = 1.5\times 10^{25}\rho T_s^{-7/2}\frac{1-e^{-x}}{x^3}g(x,T)\ (\text{cm}^2\ \text{g}^{-1})\ , \tag{50}$$

where $x = h\nu/kT$ and $g(x,T) \approx 1$. Equation (49) shows that κ_T is constant, i.e. it does not depend neither on frequency nor on the disc properties. On the other hand, κ_{ff} depends strongly on the disc temperature and density. It also decreases strongly with increasing frequency, which means that κ_{ff} may dominate the spectrum at low frequencies.

In principle, the spectrum can be constructed using equation (36) with I_ν instead of B_ν and following the process of section 2.7.2. However, in this case, there is not an explicit formula for

the temperature, since we cannot use the Stefan-Boltzmann law for the black body flux. The temperature, T_s, appearing in eq.(48), should be representative of the disc surface temperature. This is because the observed spectrum is formed at the thin surface layer at a distance from the surface which is less than the thermalization optical depth of one. T_s should be determined by equating the total emitted flux, meaning the integral of I_ν over all frequencies and solid angles, to the gravitational dissipation rate per unit surface area, i.e.

$$\pi \int_0^\infty I_\nu d\nu = Q \ (\mathrm{erg\ s^{-1}\ cm^{-2}}) \ . \tag{51}$$

The equation above implies that the rate of gas heating is balanced by the cooling rate of the radiative process, and is called the energy balance equation. The π factor emerges from the assumption that each disc annulus radiates uniformly, i.e. from the integration

$$\int I_\nu \cos\theta d\Omega = I_\nu \int_0^{2\pi} \int_0^{\pi/2} \cos\theta \ \sin\theta d\theta d\phi = \pi I_\nu \ . \tag{52}$$

Substituting the expressions for I_ν and Q in eq.(51) we get

$$\frac{4\pi h}{c^2} \int_0^\infty \frac{\nu^3 d\nu}{(e^{h\nu/kT_s} - 1)(1 + \sqrt{1 + \kappa_\tau/\kappa_{ff}})} = \frac{3}{8\pi} \frac{GM\dot{M}}{R^3} \Big(1 - \sqrt{\frac{3R_s}{R}}\Big) \ . \tag{53}$$

We perform the change of variables $x \equiv h\nu/kT_s$, $r \equiv R/R_s$, $\dot{m} \equiv \eta \dot{M} c^2/L_{Edd}$ to find

$$4\pi \frac{k^4 T_s^4(r)}{h^3 c^2} \int_0^\infty \frac{x^3 dx}{(e^x - 1)(1 + \sqrt{1 + \kappa_\tau/\kappa_{ff}})} = \frac{m_p c^3}{\sigma_\tau R_s} \frac{3}{8} r^{-3} \dot{m} (1 - \sqrt{\frac{3}{r}}) \tag{54}$$

To solve the equation above for the disc surface temperature at each radius we need κ_{ff}, which depends on the disc density $\rho(r)$. In the next section we show how to calculate $\rho(r)$.

3.2 Calculation of the disc density

In this section, we write down equations that will help us derive an analytic expression for the disc density. These equations include the hydrostatic equilibrium in the vertical direction, the conservation of angular momentum, the equation of state, i.e. an expression for the pressure in the disc, the equation of radiative diffusion, and the energy balance.

3.2.1 Vertical structure

Since there is no flow perpendicular to the disc the equation of hydrostatic equilibrium holds

$$\frac{1}{\rho} \frac{\partial P}{\partial z} = \frac{\partial}{\partial z} \Big[\frac{GM}{(R^2 + z^2)^{1/2}} \Big] \ , \tag{55}$$

where z is the vertical extend of the disc. This equation states that the pressure gradient is balanced by the vertical gradient of the gravitational potential of the central massive object. Taking the derivative we find

$$\frac{1}{\rho} \frac{\partial P}{\partial z} = - \frac{GMz}{(R^2 + z^2)^{3/2}} \ . \tag{56}$$

If we assume that the disc is vertically thin, which means that $R \gg z$, then

$$\frac{1}{\rho}\frac{\partial P}{\partial z} = -\frac{GM}{R^3}z\,. \tag{57}$$

Under the same assumption we can write

$$\frac{\partial P}{\partial z} \approx \frac{P(H) - P(0)}{H} \approx -\frac{P(0)}{H}\,, \tag{58}$$

since $P(0) \gg P(H)$. If we also assume that the disc pressure does not vary with depth, then

$$P = \rho\frac{GM}{R^3}H^2\,. \tag{59}$$

This is an expression that connects pressure, density and the disc height at each radius.

3.2.2 Conservation of angular momentum

In Chapter 2 we found the following expression for the surface density of the disc

$$\Sigma(R) = \frac{\dot{M}}{3\pi\nu}\Big(1 - \sqrt{\frac{3R_s}{R}}\Big)\,. \tag{60}$$

The equation above includes the viscosity of the disc, which we assume is equal to $\nu = \alpha c_s H$, and $\alpha = 0.1$. The sound speed in the medium is given by $c_s^2 = P/\rho$. If we further assume that the disc density does not vary considerably with z then, using the definition of the surface density, i.e.

$$\Sigma = \int_0^H \rho dz \approx \rho H\,, \tag{61}$$

we can find an additional equation between P, ρ and H by substituting ν, c_s and Σ into eq.(60), as follows

$$H^2\sqrt{P\rho} = \frac{\dot{M}}{3\pi\alpha}\Big(1 - \sqrt{\frac{3R_s}{R}}\Big)\,. \tag{62}$$

At this point, we have two equations, eq.(59) and eq.(62), but three unknown quantities, namely H, P, ρ. The next step then, is to derive an expression for the pressure.

3.2.3 Equation of state

The pressure in the disc is due to gas and radiation. Assuming ideal gas, we have

$$P_{gas} = nkT\,, \tag{63}$$

where T is equal to the average temperature along the z axis, n is the number of particles per unit volume, k the Boltzmann constant, and we have assumed that the effects of the temperature change with depth are not important. We can use $n = \rho/\mu m_p$ to eliminate n and get

$$P_{gas} = \frac{\rho kT}{\mu m_p}\,, \tag{64}$$

where μ is the mean mass per particle measured in units of hydrogen mass m_H. It is called the mean molecular mass, and is equal to 1 for neutral hydrogen, while for ionized hydrogen it is equal to 1/2. In our case, we will use $\mu = 1/2$.

The radiation pressure is, assuming black body radiation,

$$P_{rad} = \frac{4\sigma T^4}{3c} \ . \tag{65}$$

Therefore the total pressure will be

$$P = \frac{2\rho k T}{m_p} + \frac{4\sigma T^4}{3c} \, . \tag{66}$$

We have derived three equations that connect the height, the pressure, the density and the temperature of the disc. To solve for the density we need an extra equation that can be found by considering the diffusive radiation transport equation along the z-axis.

3.2.4 Radiative transfer

We start from the Rosseland approximation for the total energy flux, $F(z)$ (i.e. $I_\nu(z)$ integrated over all frequencies at each z), as it is transported along the disc height, also known as the equation of radiative transfer:

$$F(z) = -\frac{16\sigma T^3}{3\alpha_R}\frac{\partial T}{\partial z} \ , \tag{67}$$

where α_R is the Rosseland mean absorption coefficient, which is a weighted average of the absorption and scattering coefficients over all frequencies, and is equal to $\alpha_R = \rho\kappa_R$, where κ_R is the Rosseland mean opacity.

Since $\partial T^4/\partial z = 4T^3 \partial T/\partial z$, and

$$\frac{\partial T^4}{\partial z} \approx \frac{T^4(z=H,r) - T^4(z=0,r)}{H-0} \approx \frac{-T^4(z=0,r)}{H} \ , \tag{68}$$

then, eq.(67) becomes

$$F = \frac{4\sigma}{3\alpha_R H} T^4 \, . \tag{69}$$

Since the optical depth of the disc is given by

$$\tau_d = \rho H \kappa_R \ , \tag{70}$$

eq.(69) becomes

$$F = \frac{4\sigma}{3\tau_d} T^4 \, . \tag{71}$$

As we already said, the main contributions to the opacity of the disc come from free-free absorption and electron scattering. According to Frank, King & Raine (1992), the Rosseland mean opacity can be well approximated by the Kramer's law,

$$\kappa_R = 6.6 \times 10^{22} \rho T^{-7/2} \ (\mathrm{cm}^2 \ \mathrm{g}^{-1}) \ , \tag{72}$$

at radii,

$$R \geq 4.3 \times 10^{-14} \dot{M}^{2/3} M^{1/3} \Big(1 - \sqrt{\frac{3R_s}{R}}\Big)^{2/3} \ . \tag{73}$$

At smaller radii the most important contribution is Thomson scattering, i.e.

$$\kappa_R \approx \kappa_T = 0.4 \ (\mathrm{cm}^2 \ \mathrm{g}^{-1}) \ . \tag{74}$$

For a typical AGN with a black hole of mass $M = 10^7 M_\odot$ and accretion rate $\dot{m} = 0.05$, which translates to $\dot{M} = 1.26 \times 10^{24}$g/s, we find that free-free absorption dominates at radii larger than $1.36 \times 10^{16}\mathrm{cm} = 4530 R_s$. Larger accretion rates and more massive black holes imply that the disc region where opacity will be mainly determined by free-free absorption extends further out, as we can tell from eq.(73). Therefore, for a disc that extends up to $5000 R_s$, we assume that Thomson scattering is the main opacity source throughout the disc. Then the optical depth can be written as

$$\tau_d = \rho H \kappa_T = \rho H \sigma_T / m_p \ . \tag{75}$$

Since we derived an expression that connects the temperature with the energy flux, all that is left is the energy balance equation

$$F = Q \Rightarrow \frac{4\sigma}{3\tau_d} T^4 = \frac{3}{8\pi} \frac{GM\dot{M}}{R^3} \Big(1 - \sqrt{\frac{3R_s}{R}}\Big) \, . \tag{76}$$

Now, the system of the disc equations is completed. We list all of them below:

$$P = \rho \frac{GM}{R^3} H^2 \ , \tag{77}$$

$$H^2 \sqrt{P\rho} = \frac{\dot{M}}{3\pi\alpha} \Big(1 - \sqrt{\frac{3R_s}{R}}\Big) \ , \tag{78}$$

$$P = \frac{2\rho k T}{m_p} + \frac{4\sigma T^4}{3c} \, , \tag{79}$$

$$\frac{4\sigma}{3\tau_d} T^4 = \frac{3}{8\pi} \frac{GM\dot{M}}{R^3} \Big(1 - \sqrt{\frac{3R_s}{R}}\Big) \, , \tag{80}$$

$$\tau_d = \frac{\rho H \sigma_T}{m_p} \ . \tag{81}$$

We can use the above equations to compute $\rho(r)$, which we will use to compute κ_{ff}, according to eq.(50), and T_s from eq.(54). We solve below the equations above in the case when either the gas pressure or the radiation pressure is the dominant pressure component in the disc.

3.3 The radiation pressure dominated solutions

First we consider the disc region where $P_{rad} \gg P_{gas}$, which means that $P \approx 4\sigma T^4/3c$. Here, we present the solutions for $H/R, P, \rho, T$, and τ_d, as a function of radius. Their derivation is shown in Appendix A. The solutions are as follows:

$$\frac{H}{R}(r) = \frac{3}{4} r^{-1} (\dot{m}/\eta) J(r) \ , \tag{82}$$

$$\rho(r) = \frac{128\sqrt{2}}{81} \frac{m_p}{\sigma_T R_s} \alpha^{-1} r^{3/2} [(\dot{m}/\eta) J(r)]^{-2} = 1.9 \times 10^{-13} (\alpha M_8)^{-1} r^{3/2} [(\dot{m}/\eta) J(r)]^{-2} \ (\mathrm{g \ cm}^{-3}) \ , \tag{83}$$

$$P(r) = P_{rad}(r) = \frac{4\sqrt{2}}{9}\frac{m_p c^2}{\sigma_T R_s}\alpha^{-1} r^{-3/2} = 4.8\times 10^7 (\alpha M_8)^{-1} r^{-3/2}\ (\mathrm{g\ cm^{-1}\ s^{-2}})\ , \tag{84}$$

$$T(r) = \Big(\frac{\sqrt{2}}{3}\frac{c^3 m_p}{\sigma\sigma_T R_s}\Big)^{1/4}\alpha^{-1/4} r^{-3/8} = 3.72\times 10^5 (\alpha M_8)^{-1/4} r^{-3/8}\ (\mathrm{K})\ , \text{and} \tag{85}$$

$$\tau_d(r) = \frac{32\sqrt{2}}{27}\alpha^{-1} r^{3/2}[(\dot{m}/\eta)J(r)]^{-1}\ , \tag{86}$$

where $J(r) = 1-\sqrt{3/r}$, $M_8 = M/(10^8 M_\odot)$.

Let us, also, calculate the effective optical thickness of the medium defined as $\tau_{eff} = \sqrt{\tau_a(\tau_a+\tau_s)}$, where $\tau_a = \kappa_{ff}\rho H$ and $\tau_s = \kappa_T \rho H$ are the absorption and scattering optical thickness respectively. Since Thomson scattering is the main contribution to opacity we can make the approximation $\tau_{eff} \approx \sqrt{\tau_a \tau_s}$. We compute τ_a using eq.(72), eq.(83) and eq.(85) and τ_s from eq.(86) to find

$$\tau_{eff}(r) = 5.31\times 10^{-5}\alpha^{-17/16} M_8^{-1/16} r^{93/32}[(\dot{m}/\eta)J(r)]^{-2}\ . \tag{87}$$

When $\tau_{eff} \ll 1$ the medium is said to be effectively thin. This means that most photons can escape the medium by random walking before they are absorbed. On the contrary, when $\tau_{eff} \gg 1$ the medium is effectively thick and thus we have thermal equilibrium between radiation and matter.

Lastly, we calculate the radiation to gas pressure ratio so we can identify the disc region where radiation pressure dominates. Since the gas pressure is given by eq.(60), then the ratio is

$$\begin{aligned}\frac{P_{rad}}{P_{gas}} &= \frac{9}{64}\Big(\frac{3\sqrt{2}}{2}\Big)^{1/4}\frac{1}{k}(\sigma\sigma_T R_s m_p^3 c^5)^{1/4}\alpha^{1/4} r^{-21/8}[(\dot{m}/\eta)J(r)]^2 \\ &= 41.2\times 10^5 (\alpha M_8)^{1/4} r^{-21/8}[(\dot{m}/\eta)J(r)]^2\ .\end{aligned} \tag{88}$$

Equations (82)-(88) have been derived assuming that radiation pressure dominates, therefore they are valid only when the ratio is greater than unity, i.e. $P_{rad}/P_{gas} > 1$.

3.4 The gas pressure dominated solutions

When $P_{gas} \gg P_{rad}$ the solutions become

$$\frac{H}{R}(r) = 1.7\times 10^{-3}(\alpha M_8)^{-1/10} r^{1/20}[(\dot{m}/\eta)J(r)]^{1/5}\ , \tag{89}$$

$$\rho(r) = 1.65\times 10^{-5}(\alpha M_8)^{-7/10} r^{-33/20}[(\dot{m}/\eta)J(r)]^{2/5}\ (\mathrm{g\ cm^{-3}})\ , \tag{90}$$

$$P(r) = P_{gas}(r) = 2.13\times 10^{10}(\alpha M_8)^{-9/10} r^{-51/20}[(\dot{m}/\eta)J(r)]^{4/5}\ (\mathrm{g\ cm^{-1}\ s^{-2}})\ , \tag{91}$$

$$T(r) = 7.8\times 10^6 (\alpha M_8)^{-1/5} r^{-9/10}[(\dot{m}/\eta)J(r)]^{2/5}\ (\mathrm{K})\ , \text{and} \tag{92}$$

$$\tau_d(r) = 3.28\times 10^5 \alpha^{-4/5} M_8^{1/5} r^{-3/5}[(\dot{m}/\eta)J(r)]^{3/5}\ , \tag{93}$$

$$\tau_{eff}(r) = 473\alpha^{-4/5} M_8^{1/5} r^{3/20}[(\dot{m}/\eta)J(r)]^{1/10}\ . \tag{94}$$

The radiation to gas pressure ratio in this case is

$$\frac{P_{rad}}{P_{gas}} = 438(\alpha M_8)^{1/10} r^{-21/20} [(\dot{m}/\eta) J(r)]^{4/5} \ . \tag{95}$$

The above ratio must be below unity for the gas dominated solutions to hold.

3.5 The pressure ratio

Figure (11) shows plots of the pressure ratio, P_{rad}/P_{gas}, for $M_8 = 0.01, 0.1, 1, 10$, and $\dot{m} = 0.005, 0.05, 0.5$. The solid red line in the top left panel of Fig.(11) shows the pressure ratio given by eq.(88), i.e. when radiation pressure dominates in the case of $\dot{m} = 0.05$. The dashed red line in the same panel shows the same ratio when gas pressure dominates, i.e. P_{rad}/P_{gas} calculated using eq.(95). The two lines intersect at two radii, say $r_{eq,1}$ and $r_{eq,2}$, with $r_{eq,1} \ll r_{eq,2}$ ($r_{eq,1}$ is very close to r_{isco} and it is hard to see on the plot). Both the solid and the dashed red lines show $P_{rad} > P_{gas}$ between $r_{eq,1}$ and $r_{eq,2}$, while $P_{rad} < P_{gas}$ at all other radii. This implies that the disc is radiation pressure dominated between $r_{eq,1}$ and $r_{eq,2}$, and gas pressure dominated outside this region. It is for this reason that we plot the radiation pressure dominated solutions between $r_{eq,1}$ and $r_{eq,2}$ in all panels of Fig.(11), and the gas pressure solutions at all other radii. Figure (11) also shows that $r_{eq,2}$ increases with increasing $\dot{m}$. Below a certain small accretion rate, the gas pressure should dominate at all radii. At the same time, for a given accretion rate, $r_{eq,2}$ appears to increase with the BH mass as well.

The radii $r_{eq,1}$ and $r_{eq,2}$ should be the solutions to the equation $P_{rad} = P_{gas}$, or equivalently $P_{rad}/P_{gas} = 1$. Using eq.(88)[1], we find

$$\begin{aligned} 41.2 \times 10^5 (\alpha M_8)^{1/4} r^{-21/8} [(\dot{m}/\eta) J(r)]^2 = 1 \Rightarrow \\ \frac{r^{21/8}}{J(r)^2} = 41.2 \times 10^5 (\alpha M_8)^{1/4} (\dot{m}/\eta)^2 \Rightarrow \\ \frac{r}{J(r)^{16/21}} = 331 (\alpha M_8)^{2/21} (\dot{m}/\eta)^{16/21} \end{aligned} \tag{96}$$

Solving eq.(96) numerically we can calculate $r_{eq,1}$, $r_{eq,2}$ for any black hole mass and sufficiently large accretion rates $\dot{m}$. For small accretion rates, we get no solutions, which means that gas pressure dominates over the whole disc. Radii $r_{eq,1}$ and $r_{eq,2}$ divide the disc into three regions. The first one is a very small annulus close to the inner edge, $r < r_{eq,1}$, where gas pressure dominates (barely visible in Fig.11). Then for $r_{eq,1} < r < r_{eq,2}$ radiation pressure is dominant, while for the rest of the disc, gas pressure prevails.

Figure (12) shows a plot of $r_{eq,1}$ and $r_{eq,2}$ versus $\dot{m}$ for all the BH masses we consider. The points at the bottom of the graph show the smaller roots $r_{eq,1}$, while the points at the top indicate the larger ones, $r_{eq,2}$. Both axes in Fig.(12) are in logarithmic scale. This implies that a power-law relation of the form

$$r_{eq,2}(\dot{m}, M_8) = A \times \big(\frac{\dot{m}}{0.05}\big)^s \ , \tag{97}$$

can describe well the dependence of $r_{eq,2}$ on M_8 and $\dot{m}$. If we take the logarithm of each side of eq.(97), then we get

$$log(r_{eq,2}) = logA + s \times log(\frac{\dot{m}}{0.05}) \ . \tag{98}$$

[1]We could also arrive to the same result by solving $P_{rad}/P_{gas} = 1$ using eq.(95), or even setting eq.(84) equal to eq.(91).

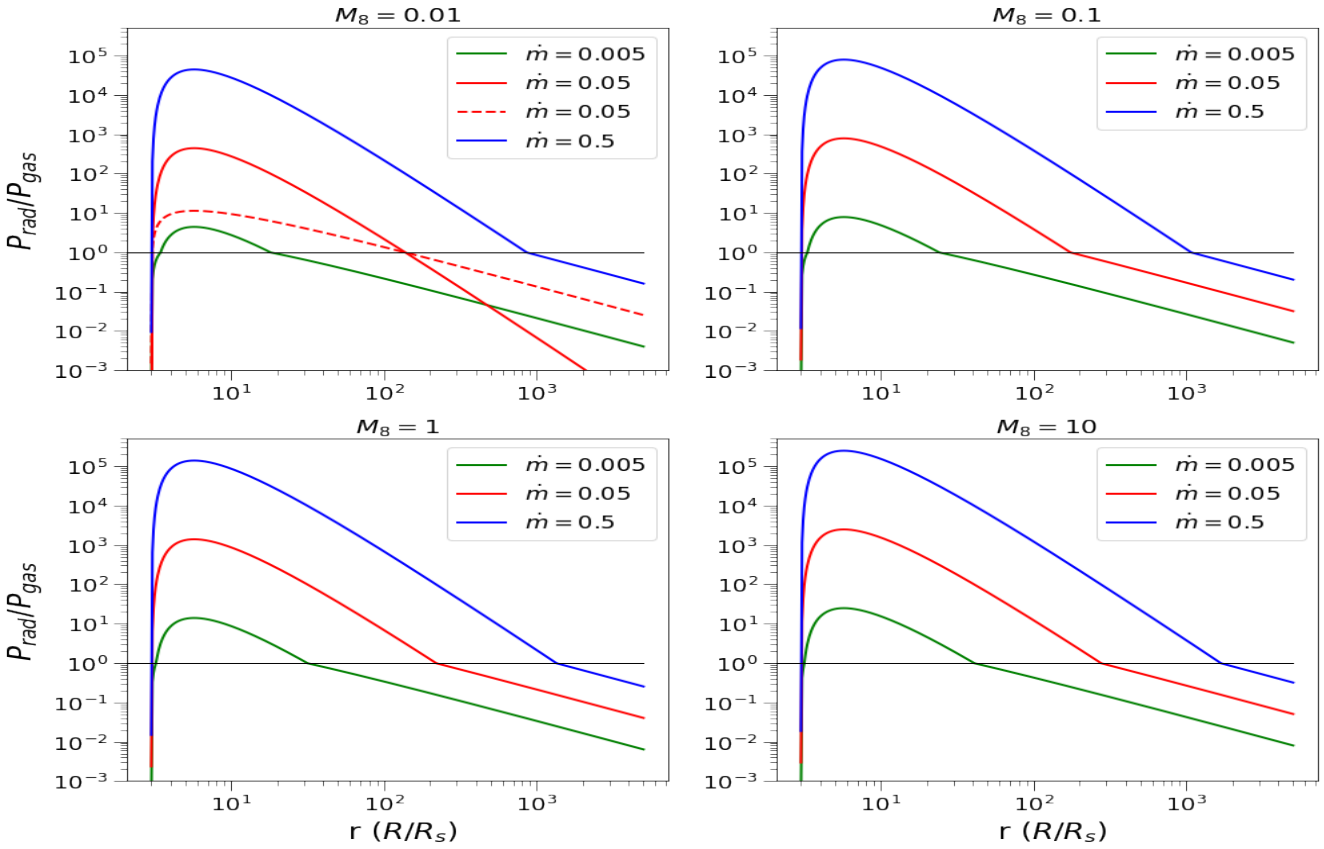

Figure 11: Pressure ratio P_{rad}/P_{gas} for black hole masses $M_8 = 0.01, 0.1, 1, 10$ and accretion rates $\dot{m} = 0.005, 0.05, 0.5$.

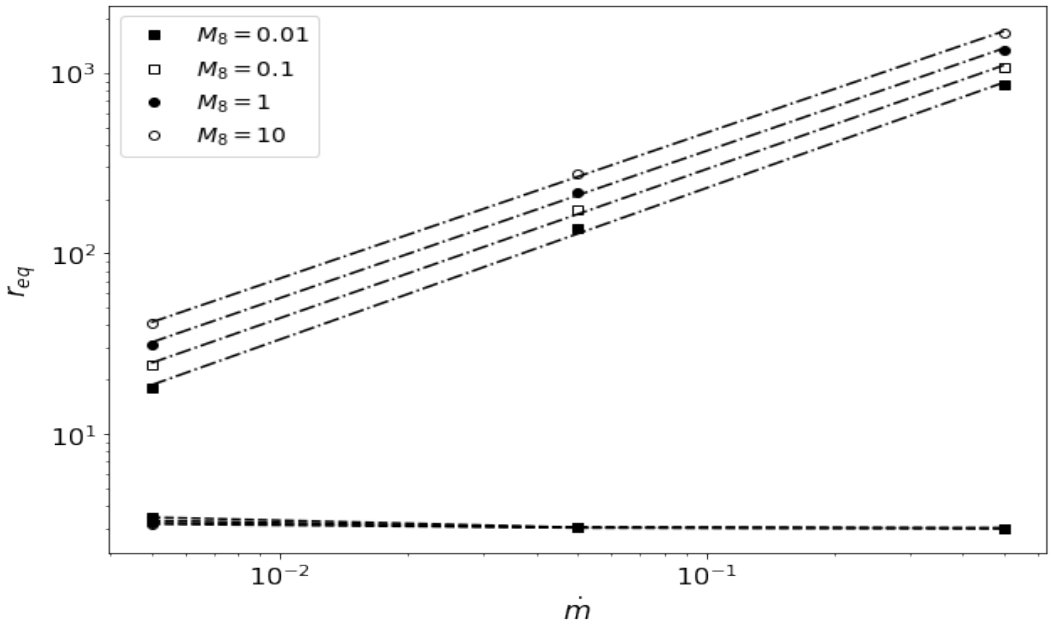

Figure 12: The radius r_{eq} as a function of the accretion rate $\dot{m}$ for black holes of different masses. Points at the bottom indicate $r_{eq,1}$, while points at the top indicate $r_{eq,2}$. The dot-dashed lines are the best-fit lines (99)-(102). The dashed lines simply connect the $r_{eq,1}$ points.

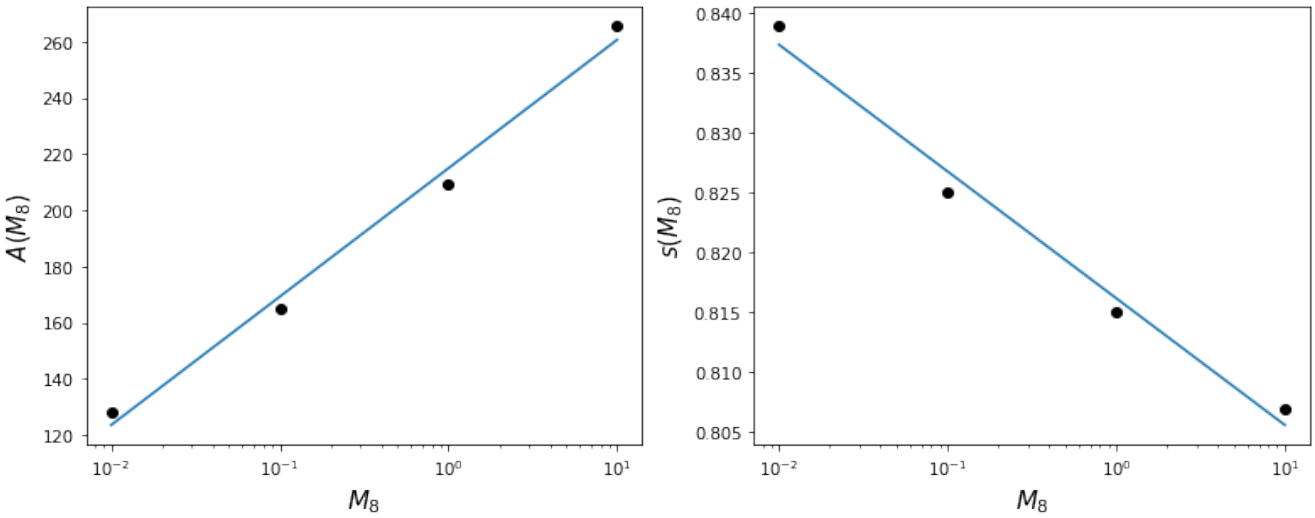

Figure 13: A, s as function of M_8. Solid lines show the best fit models to the data.

We therefore fit a straight line to the data plotted in Fig.(12) to determine A, s. The best fit results are as follows:

$$r_{eq,2}(\dot{m}, M_8 = 0.01) = 128.4 \times \left(\frac{\dot{m}}{0.05}\right)^{0.839} \tag{99}$$

$$r_{eq,2}(\dot{m}, M_8 = 0.1) = 164.9 \times \left(\frac{\dot{m}}{0.05}\right)^{0.825} \tag{100}$$

$$r_{eq,2}(\dot{m}, M_8 = 1) = 209.6 \times \left(\frac{\dot{m}}{0.05}\right)^{0.815} \tag{101}$$

$$r_{eq,2}(\dot{m}, M_8 = 10) = 265.8 \times \left(\frac{\dot{m}}{0.05}\right)^{0.807} , \tag{102}$$

and the respective best fit models are plotted with the dot-dashed lines in Fig.(12). We notice that A increases for larger M_8, while s decreases. To study this behaviour we plot A and s as a function of M_8 in Figure (13). The figure shows that there is a linear relation between these two parameters and $log(M_8)$. We therefore fitted the data plotted in Fig.(13) with lines of the form

$$A(M_8) = c_1 \times log(M_8) + c_2 \tag{103}$$

$$s(M_8) = c_3 \times log(M_8) + c_4 , \tag{104}$$

The best fit results are as follows:

$$A(M_8) = 45.69 \times log(M_8) + 215.02 \tag{105}$$

$$s(M_8) = -0.0106 \times log(M_8) + 0.8162 , \tag{106}$$

and the solid lines in Fig.(13) show these best-fit lines. Clearly, both $A(M_8)$ and $s(M_8)$ are well described by equations (105) and (106), respectively.

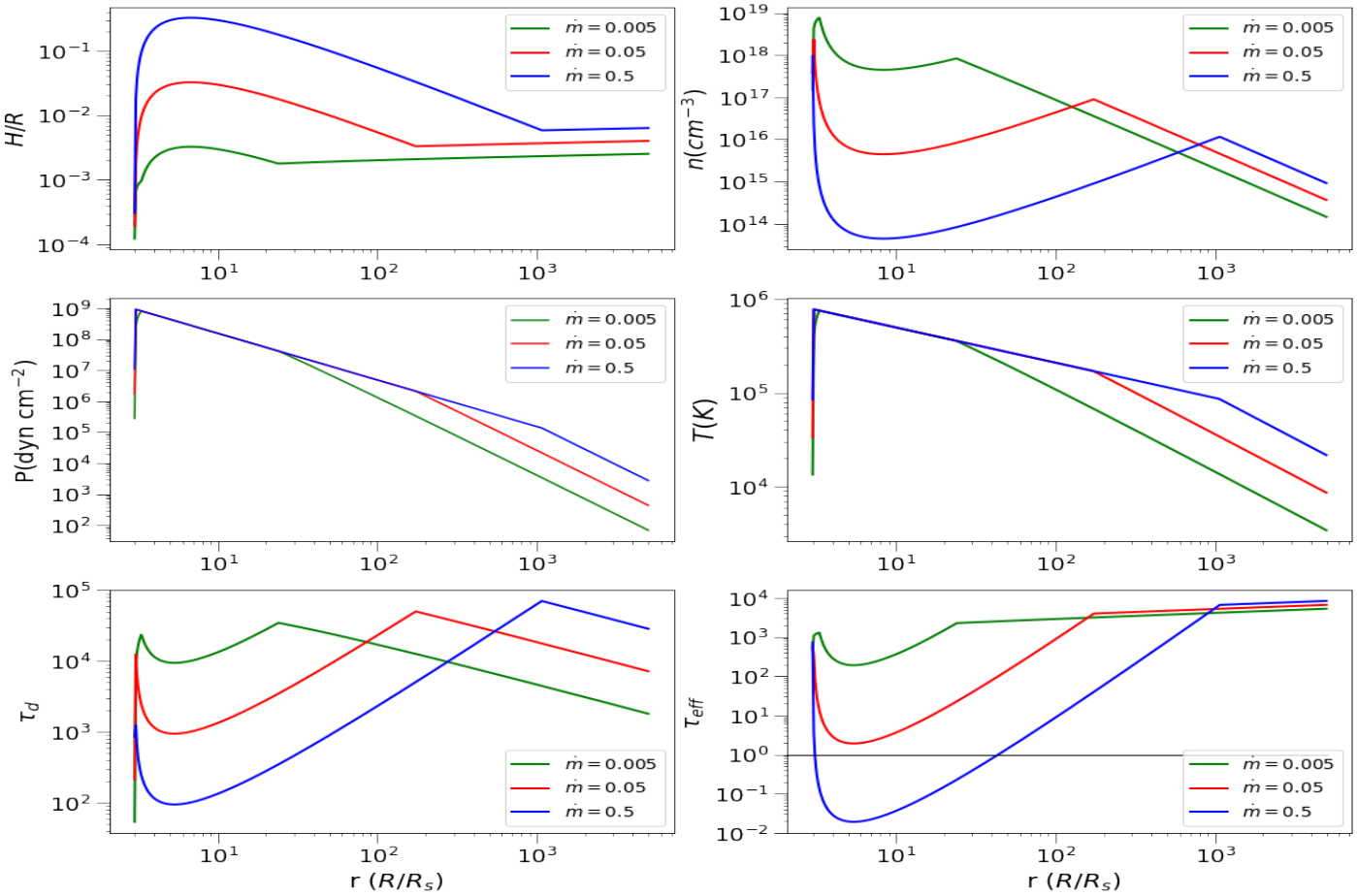

Figure 14: $H/R, n, P, T, \tau_d, \tau_{eff}$ for a black hole of mass $M_8 = 0.1$ and accretion rates $\dot{m} = 0.005, 0.05, 0.5$

3.6 The disc parameters

Figure (14) shows plots of the disc parameters $H/R, n, P, T, \tau_d$ and τ_{eff} as a function or r. These plots were computed using eqs.(82)-(87) when $P_{rad} > P_{gas}$ and eqs.(89)-(94) when $P_{gas} > P_{rad}$. The radii $r_{eq,1}$, $r_{eq,2}$ which determine the radiation/gas pressure dominated regions were calculated using eq.(96).

On the top left panel, we present the ratio $\frac{H}{R}(r)$. We notice that when radiation pressure dominates the ratio rises significantly. This increase in vertical thickness takes up a larger part of the disc as the accretion rate increases. This is because the radiation zone expands as mentioned before. We note that the highest values of H/R are of order $0.1 - 0.2$, which are still consistent with the thin disc approximation. The top right panel shows the number density, n, as a function of the radius. The number density is equal to the mass density ρ divided by the proton mass m_p and multiplied by 2, to take into account the electrons from the ionized hydrogen. It decreases logarithmically with increasing radius in the gas pressure dominated part of the disc. It also decreases considerably in the radiation pressure part, where H/R increases significantly.

The middle panels show the pressure and the temperature radial profiles. The disc pressure and temperature are maximum at a radius very close to r_{isco}. As radius increases, both quantities drop as power laws of r (with pressure dropping faster than temperature). This is because the dissipation rate of the gravitational energy, Q, decreases as we move outwards. This leads to smaller temperatures at the outer disc. Since pressure is proportional to temperature it will present the same behaviour. Temperature and pressure increase for larger accretion rates. This can be explained by the increase of Q, since it is directly proportional to $\dot{m}$, as we can see in eq.(28). It is worth mentioning that the dependence on the accretion rate disappears for both the temperature and the pressure when radiation is dominant. This probably happens because the work that the torques do is used to expand the disc, as the top left panel in Fig.(14) shows, instead of being dissipated as heat.

The bottom panels show the disc optical depth. Both τ_d and τ_{eff} drop significantly when radiation dominates since the disc becomes less dense, leading to fewer interactions between photons and matter. Despite that, the scattering optical depth greatly exceeds unity for all r, meaning that the disc is optically thick for Thomson scattering. For the effective optical depth, however, we notice that when $\dot{m} = 0.5$ the disc becomes effectively thin. This means that photons from these parts of the disc can escape before being absorbed or scattered. This happens inside a small part of the radiation pressure zone, extending from $r \approx 3.1$ to $r \approx 44$. The rest of the radiation zone is effectively thick for all $\dot{m}$.

Plots of the disc parameters as a function of radius are similar for other BH masses as well. The black hole mass is merely altering the extent of the radiation zone, while the qualitative shape of the disc parameters plots remains the same.

3.7 Computation of the modified disc spectrum

3.7.1 The surface temperature profile

Before we calculate the disc energy spectrum we need to calculate the surface temperature of the disc. This is done as follows:

1. we split the disc into 265 annuli (each annulus has an inner radius r_i and an outer radius r_{i+1}), just like we did in section 2.7.1,

2. we calculate the radii where $P_{rad} = P_{gas}$, using eq.(96),

3. we solve eq.(54) numerically for each radius r_i, using the *fsolve* function of the python library *scipy*. To solve for T_s, we must calculate the expression

$$4\pi\frac{k^4T_s^4}{h^3c^2}\int_0^\infty \frac{x^3dx}{(e^x-1)(1+\sqrt{1+\kappa_\tau/\kappa_{ff}(x,\rho,T_s)})} = \frac{m_pc^3}{\sigma_\tau R_s}\frac{3}{8}r^{-3}\dot{m}(1-\sqrt{\frac{3}{r}}) \ . \tag{107}$$

The integral of the above expression is computed over the interval $[0.01, 20]$ using the trapezoidal rule, i.e.

$$\int_0^\infty f(x)dx \approx \int_{0.01}^{20} f(x)dx = \sum_{i=0}^{N}\frac{f(x_{i+1})+f(x_i)}{2}\Delta x_i \ , \tag{108}$$

where $\Delta x_i = x_{i+1} - x_i$ and

$$f(x) = \frac{x^3}{(e^x-1)(1+\sqrt{1+\kappa_\tau/\kappa_{ff}(x,\rho,T_s)})} \ . \tag{109}$$

In our case, N=99, and the points x_i are calculated by $\log(x_i) = \log(x_{low}) + i[\log(x_{high}) - \log(x_{low})]/100$, with $x_{low} = 0.01$ and $x_{high} = 20$. We note that $f(x)$ falls off very quickly for very small and large x, and it is for this reason that the interval $[0.01, 20]$ is a good approximation of $[0, \infty]$. The function $f(x)$ also depends on κ_{ff} and therefore the disc density. At radii $r_{eq,1} < r_i < r_{eq,2}$ we compute the density using eq.(83), while for $r_i < r_{eq,1}$, $r_i > r_{eq,2}$ we use eq.(90).

Figure (15) shows a plot of T_s as a function of the radius for $M = 10^7 M_\odot$ and $\dot{m} = 0.05$. The vertical dashed lines indicate the radii where $P_{rad} = P_{gas}$. In this case, $r_{eq,1} = 3.03$ and $r_{eq,2} = 174.5$. We also plot the temperature that we computed in section 2.7.1, where we assumed that the spectrum of the disc is a multi black body (mBB) spectrum . At radii $r < 50$, T_s is higher than the mBB temperature. This is expected since the black body is the most efficient emitter. At larger radii, however, the two temperatures coincide, which means that the disc spectrum at these radii is similar to the mBB spectrum.

3.7.2 The "modified" black body (MBB) disc spectrum

To calculate the MBB spectrum, we start from eq.(36) with I_ν instead of B_ν, i.e.

$$F(\nu) = \frac{2\pi}{D^2}\int_{R_{inner}}^{R_{outer}} I_\nu R dR \ . \tag{110}$$

Substituting I_ν from eq.(48) (and multiplying by the cosξ factor) we find

$$F(\nu) = \frac{8\pi h\nu^3\cos\xi}{c^2D^2}\int_{R_{inner}}^{R_{outer}} \frac{RdR}{(e^{h\nu/kT_s(R)}-1)(1+\sqrt{1+\kappa_\tau/\kappa_{ff}[\nu,T_s(R),\rho(R)]})} \ , \tag{111}$$

and changing to the dimensionless variable $r \equiv R/R_s$ we get

$$F(\nu) = \frac{8\pi h\nu^3 R_s^2\cos\xi}{c^2D^2}\int_{r_{inner}}^{r_{outer}} \frac{rdr}{(e^{h\nu/kT_s(r)}-1)(1+\sqrt{1+\kappa_\tau/\kappa_{ff}[\nu,T_s(r),\rho(r)]})} \ . \tag{112}$$

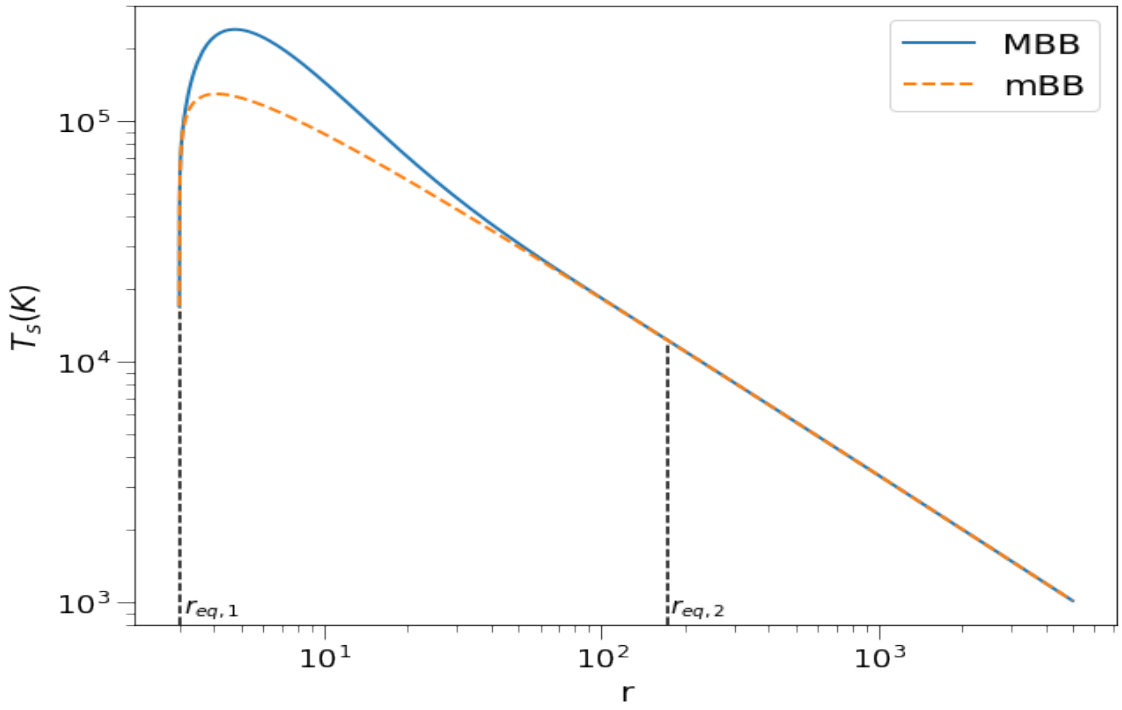

Figure 15: Temperature of a modified black body (MBB) and a multi black body (mBB) disc for accretion rate $\dot{m} = 0.05$ and central black hole mass $M = 10^7 M_\odot$.

The calculation of the spectrum is very similar to that of section 2.7.2. We consider 500 frequencies ν_i from $\nu_{low} = 10^{13} Hz$ to $\nu_{high} = 3 \times 10^{16} Hz$ with logarithmic step, using eq.(46). Then, for each frequency ν_i, we calculate the integral in eq.(112) numerically using the trapezoidal rule, i.e.

$$F(\nu_i) \approx \frac{8\pi h \nu_i^3 R_s^2 \cos\xi}{c^2 D^2} \sum_{j=0}^{264} \frac{f(r_{j+1}) + f(r_j)}{2} \Delta r_j \ , \tag{113}$$

where

$$f(r_j) = \frac{r_j}{(e^{h\nu_i / kT_s(r_j)} - 1)(1 + \sqrt{1 + \kappa_\tau / \kappa_{ff}[\nu_i, T_s(r_j), \rho(r_j)]})} \ , \tag{114}$$

$$f(r_{j+1}) = \frac{r_{j+1}}{(e^{h\nu_i / kT_s(r_{j+1})} - 1)(1 + \sqrt{1 + \kappa_\tau / \kappa_{ff}[\nu_i, T_s(r_{j+1}), \rho(r_{j+1})]})} \ . \tag{115}$$

Of course, r_j and r_{j+1} are the inner and outer radii of the same 265 annuli used previously, and Δr_j their width.

Figure (16) shows the modified black body spectrum for the case of $M = 10^7 M_\odot$, $\dot{m} = 0.05$ for an accretion disc at a distance $D = 1$Mpc and inclination $\xi = 0^o$. We also show the multi black body spectrum that we constructed in 2.7.2 for comparison. We notice that at frequencies smaller than $\sim 10^{15}$Hz, the spectra are almost identical, while the spectra differ at higher frequencies. At higher frequencies, the disc emits more power when we consider the modified black body emission. This is because the disc in this case reaches higher temperatures in the innermost rings, as we can see in Fig.(15).

We also plot the spectrum in units of $[\nu F(\nu)] = erg/sec/cm^2$ in Figure (17). From this figure we find that the maximum power of the MBB emission is $\nu F(\nu)|_{max} \approx 6.1 \times 10^{-7}$ erg/sec/cm^2 and appears at $\nu_{max} \approx 5.8 \times 10^{15}$Hz, while for the mBB power we find $\nu F(\nu)|_{max} = 7.4 \times 10^{-7}$ erg/sec/cm^2, at $\nu_{max} \approx 6.7 \times 10^{15}$Hz.

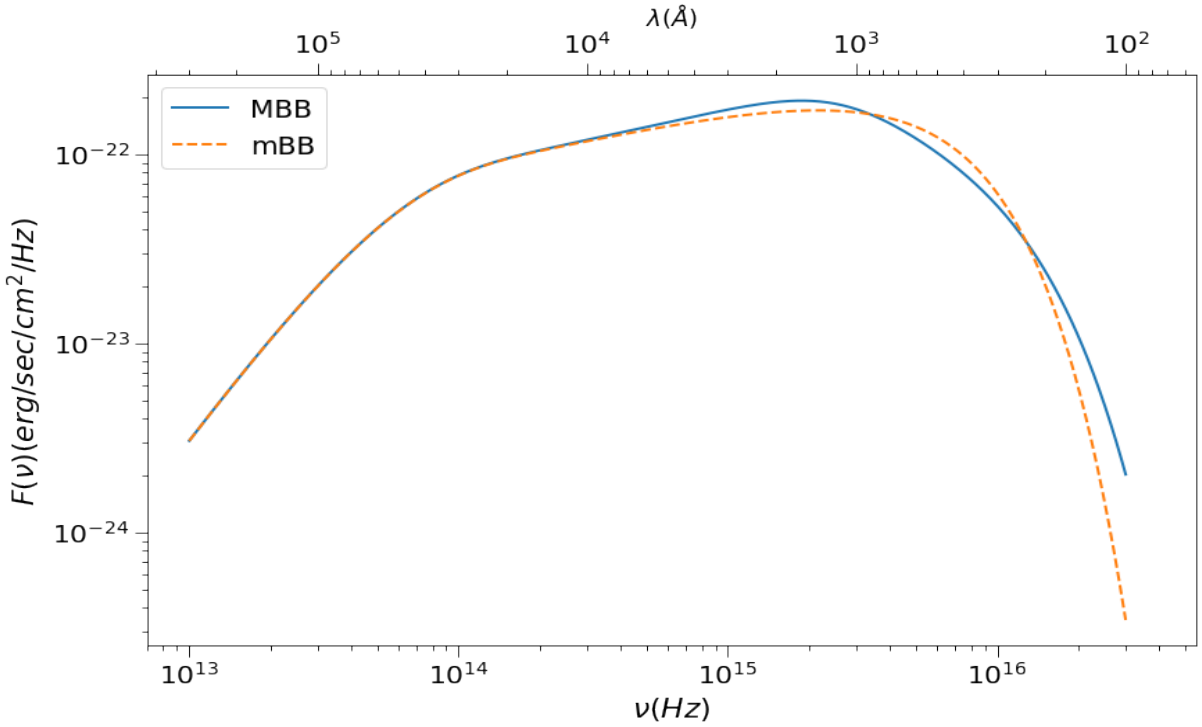

Figure 16: The modified black body (MBB) and the multi black body (mBB) disc spectrum when $\dot{m} = 0.05$ and $M = 10^7 M_\odot$.

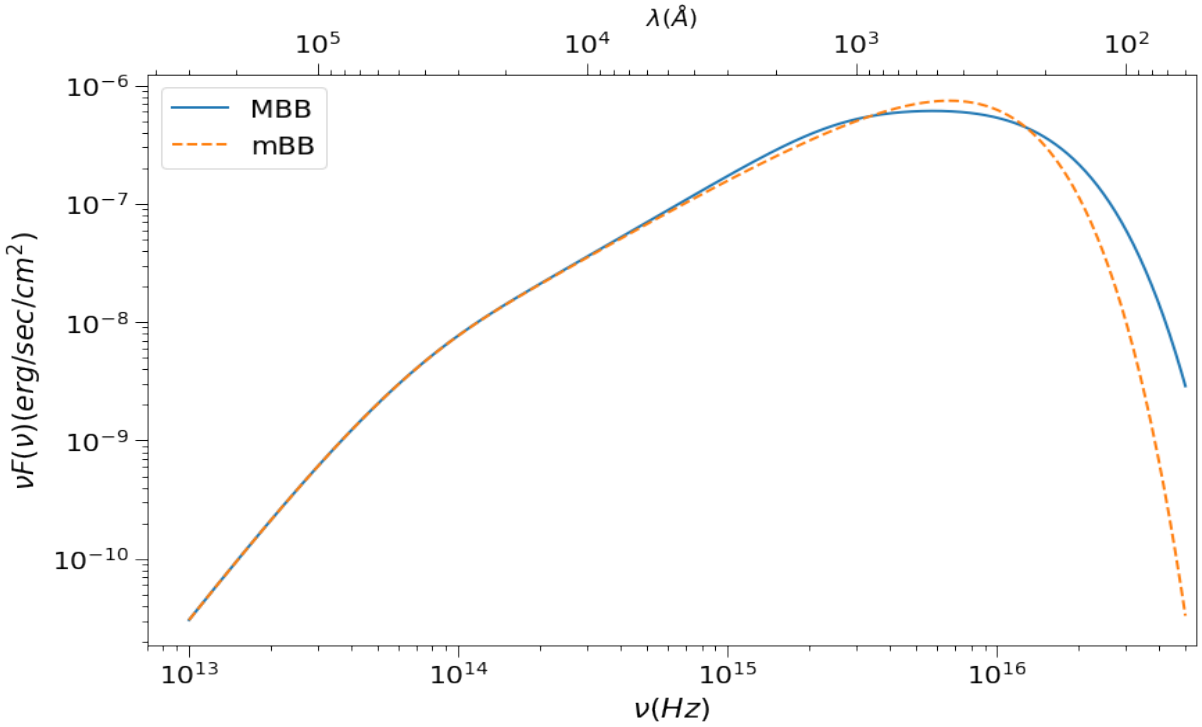

Figure 17: Same as in Fig.(16) but in $\nu F(\nu)$ units (erg/sec/cm^2).

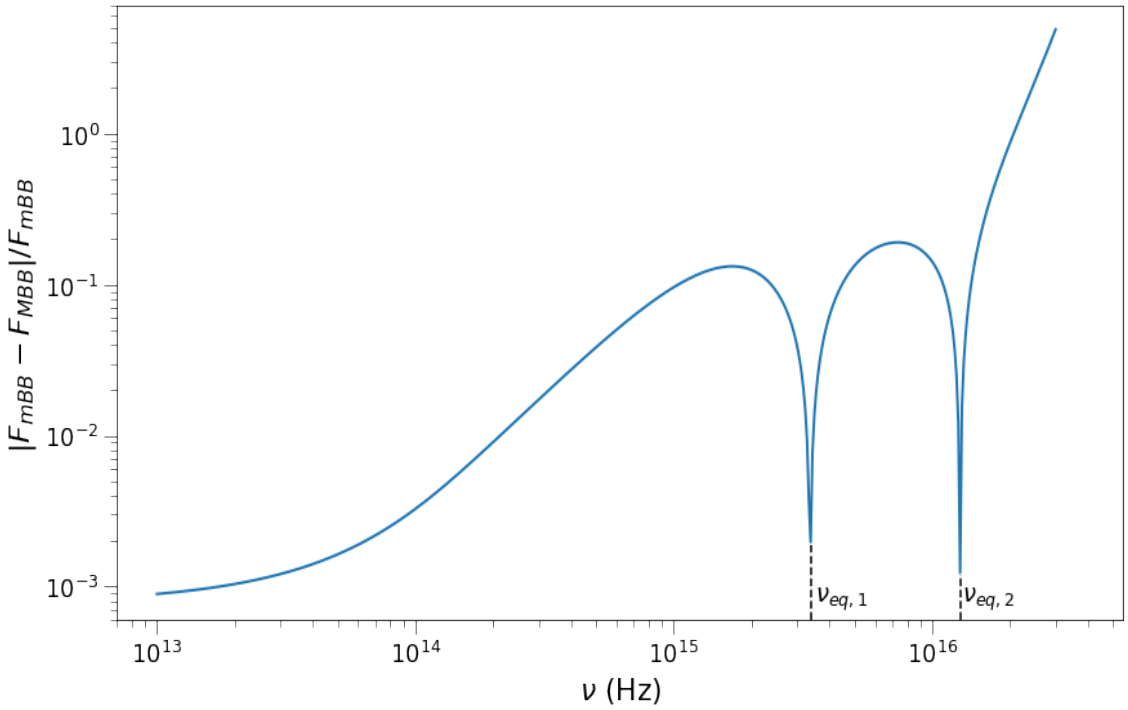

Figure 18: Relative difference $|F_{mBB} - F_{MBB}|/F_{mBB}$ between mBB and MBB spectra. The dotted lines show the frequencies where the spectra intersect ($\nu_{eq,1} = 3.38 \times 10^{15}$Hz and $\nu_{eq,2} = 1.28 \times 10^{16}$Hz).

Figure (18) shows the relative difference between the two spectra, i.e. $|F_{mBB} - F_{MBB}|/F_{mBB}$, as a function of the frequency. It is clear that at low frequencies, the differences are negligible, while they become significant at frequencies higher than $\sim 10^{15}$Hz. We also indicate the frequencies $\nu_{eq,1} = 3.38 \times 10^{15}$Hz and $\nu_{eq,2} = 1.28 \times 10^{16}$Hz where the spectra intersect.

To get a better understanding of why MBB becomes noticeably different than the mBB spectrum, Fig.(19) shows a plot of the frequency ν_0, at which $\kappa_{ff}(r, \nu_0) = \kappa_T$, as a function of the radius. As mentioned before, for $\kappa_{ff} \gg \kappa_T$ the modified spectrum approaches the black body spectrum, while the spectra differ considerably when $\kappa_T \gg \kappa_{ff}$. For frequencies higher than ν_0, κ_T is larger than κ_{ff}, since κ_{ff} is a decreasing function of frequency. Figure (19) shows that $\nu_0 > 8 \times 10^{14}$Hz at all radii. Therefore, for lower frequencies, the free-free opacity dominates at every part of the disc and thus black body emission is a good approximation for the spectrum of each disc annulus. At higher frequencies, the spectrum begins to deviate from the black body one as κ_T becomes the main contribution to opacity.

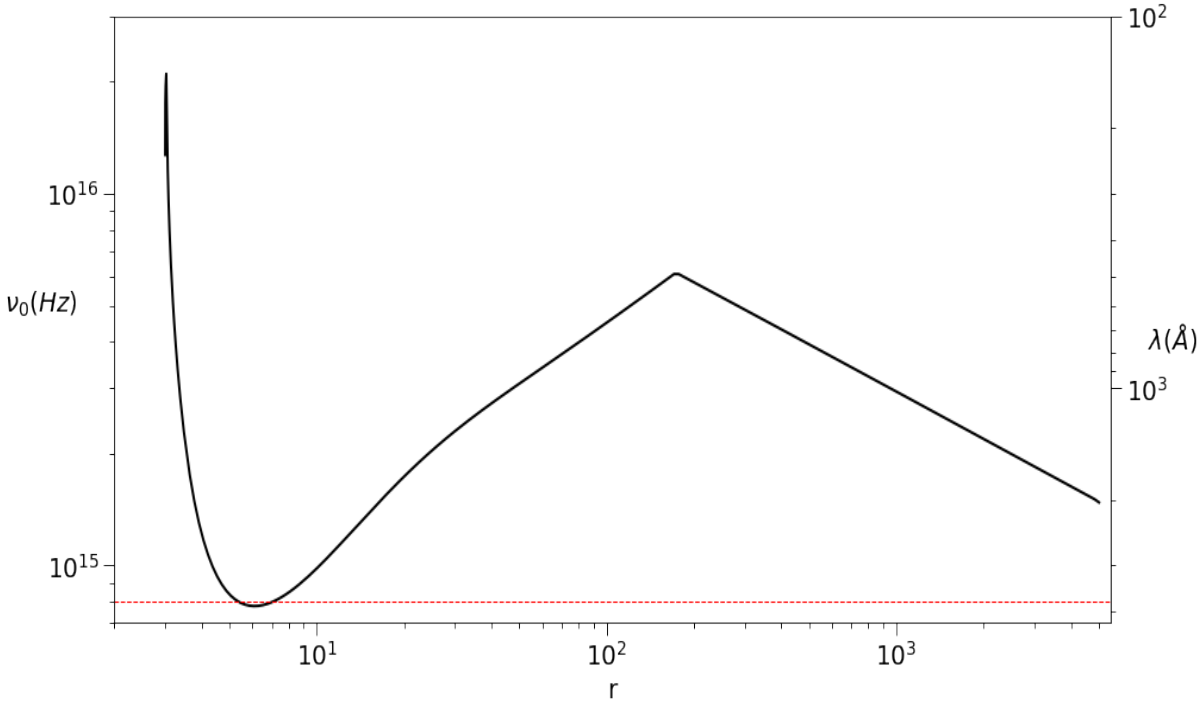

Figure 19: The frequency ν_0 for which the free-free opacity and the Thomson opacity become equal, $\kappa_{ff}(r, \nu_0) = \kappa_T$, as a function of the disc radius. The red dashed line indicates the frequency $\nu = 8 \times 10^{14}$Hz.

Chapter 4: The f parameter

4.1 Introduction

So far, we have assumed that all the gravitational power released by accretion is used to heat the disc, and is ultimately radiated away. However, AGN can be strong X-ray emitters, and can produce powerful outflows, which may carry a substantial kinetic power. Both the X-ray emission and the outflows could be powered by the energy released by accretion in the disc. In this section, we study the disc structure and the resulting disc spectrum when a fraction of the gravitational power is given to the previously mentioned effects.

For this reason, we introduce the dimensionless parameter f, which represents the fraction of the power that is not dissipated to the disc. The rest of the gravitational energy, i.e. fraction $(1-f)$, is dissipated in the disc itself and is radiated away. In effect, in the previous chapters we studied the disc spectrum assuming that $f=0$ throughout the disc. As a result, all power was radiated away, producing the disc spectrum. Here, we will consider cases where $f \neq 0$.

Generally, f does not have to be constant throughout the disc. In the inner region, f can be close to unity, while in the outer part it may approach zero. To better understand how f may vary with radius, we consider the parameter

$$A(r) = \int_{r_{in}}^{r} Q(r) 2\pi r dr \Big/ \int_{r_{in}}^{r_{out}} Q(r) 2\pi r dr \ , \tag{116}$$

where $r_{in}=3$ and $r_{out}=5000$. $A(r)$ equals the gravitational power that is dissipated up to a radius r, divided by the total gravitational power released by accretion. Substituting the expression of $Q(r)$, from eq.(54), into eq.(116) we find

$$A(r) = \int_{3}^{r} r^{-2} J(r) dr \Big/ \int_{3}^{5000} r^{-2} J(r) dr = 0.11 \int_{3}^{r} r^{-2} J(r) dr \ . \tag{117}$$

We notice that $A(r)$ is independent of the BH mass and the accretion rate, and depends solely on the radius r and the inner and outer radius of the disc.

Figure (20) shows $A(r)$ as a function of r. We calculated $A(r)$ at 1000 radii in the interval $[3, 50]$ with logarithmic step. The dashed lines in this figure show the radii at which $A(r)$ equals 1%, 5%, 10%, 20%, and 50%. We observe that A approaches unity fairly quickly. This is because most of the gravitational energy is released from accretion in the inner parts of the disc.

4.2 The new disc parameters

In this chapter we compute the disc energy spectrum for various cases of $f \neq 0$. To do this we need to calculate the disc parameters, T_s, ρ, as we explained in the previous chapter. The introduction of f will alter the equations that determine the disc parameters. More precisely, when $f \neq 0$ the energy balance equation, given in (80), becomes,

$$\frac{4\sigma}{3\tau_d} T^4 = [1-f(R)] \frac{3}{8\pi} \frac{GM\dot{M}}{R^3} \Big(1 - \sqrt{\frac{3R_s}{R}}\Big) \, . \tag{118}$$

This reduces the available energy that the disc can radiate away. As a result, the disc parameters calculated in sections 3.3 and 3.4 change by a factor of $[1-f(r)]$ in various exponents. In the case where $P_{rad} \gg P_{gas}$ the equations (82)-(88) become

$$\frac{H}{R}(r) = \frac{3}{4} r^{-1} (\dot{m}/\eta) J(r) [1-f(r)] \ , \tag{119}$$

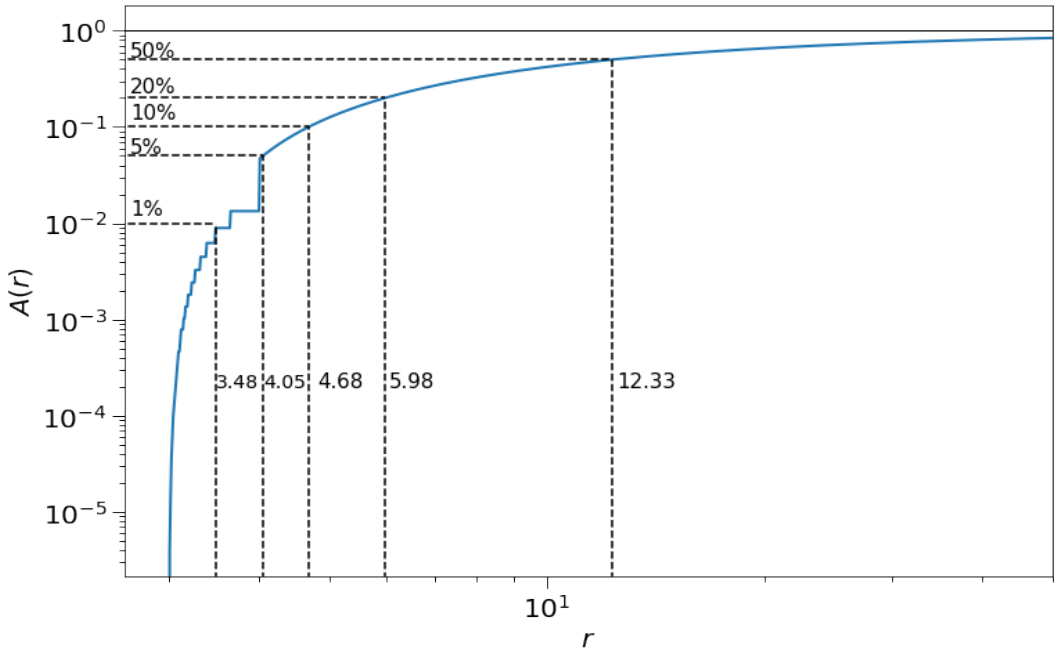

Figure 20: $A(r)$ as a function of r. The dashed lines mark the radii (in R_s) where $A(r)$ is equal to 1%, 5%, 10%, 20%, and 50%.

$$\rho(r) = 1.9 \times 10^{-13} (\alpha M_8)^{-1} r^{3/2} [(\dot{m}/\eta) J(r)]^{-2} [1 - f(r)]^{-3} \text{ (g cm}^{-3}) \,, \tag{120}$$

$$P(r) = P_{rad}(r) = 4.8 \times 10^{7} (\alpha M_8)^{-1} r^{-3/2} [1 - f(r)]^{-1} \text{ (g cm}^{-1} \text{ s}^{-2}) \,, \tag{121}$$

$$T(r) = 3.72 \times 10^{5} (\alpha M_8)^{-1/4} r^{-3/8} [1 - f(r)]^{-1/4} \text{ (K)} \,, \tag{122}$$

$$\tau_d(r) = \frac{32\sqrt{2}}{27} \alpha^{-1} r^{3/2} [(\dot{m}/\eta) J(r)]^{-1} [1 - f(r)]^{-2} \,, \tag{123}$$

$$\tau_{eff}(r) = 5.31 \times 10^{-5} \alpha^{-17/16} M_8^{-1/16} r^{93/32} [(\dot{m}/\eta) J(r)]^{-2} [1 - f(r)]^{-49/16} \,, \text{and} \tag{124}$$

$$\frac{P_{rad}}{P_{gas}} = 41.2 \times 10^{5} (\alpha M_8)^{1/4} r^{-21/8} [(\dot{m}/\eta) J(r)]^{2} [1 - f(r)]^{9/4} \,. \tag{125}$$

In the gas pressure regime, i.e. $P_{gas} \gg P_{rad}$, we find

$$\frac{H}{R}(r) = 1.7 \times 10^{-3} (\alpha M_8)^{-1/10} r^{1/20} [(\dot{m}/\eta) J(r)]^{1/5} [1 - f(r)]^{1/10} \,, \tag{126}$$

$$\rho(r) = 1.65 \times 10^{-5} (\alpha M_8)^{-7/10} r^{-33/20} [(\dot{m}/\eta) J(r)]^{2/5} [1 - f(r)]^{-3/10} \text{ (g cm}^{-3}) \,, \tag{127}$$

$$P(r) = P_{gas}(r) = 2.13 \times 10^{10} (\alpha M_8)^{-9/10} r^{-51/20} [(\dot{m}/\eta) J(r)]^{4/5} [1 - f(r)]^{-1/10} \text{ (g cm}^{-1} \text{ s}^{-2}) \,, \tag{128}$$

$$T(r) = 7.8 \times 10^6 (\alpha M_8)^{-1/5} r^{-9/10} [(\dot{m}/\eta) J(r)]^{2/5} [1 - f(r)]^{1/5} \text{ (K)} , \tag{129}$$

$$\tau_d(r) = 3.28 \times 10^5 \alpha^{-4/5} M_8^{1/5} r^{-3/5} [(\dot{m}/\eta) J(r)]^{3/5} [1 - f(r)]^{-1/5} , \tag{130}$$

$$\tau_{eff}(r) = 473 \alpha^{-4/5} M_8^{1/5} r^{3/20} [(\dot{m}/\eta) J(r)]^{1/10} [1 - f(r)]^{-7/10} \text{ , and} \tag{131}$$

$$\frac{P_{rad}}{P_{gas}} = 438 (\alpha M_8)^{1/10} r^{-21/20} [(\dot{m}/\eta) J(r)]^{4/5} [1 - f(r)]^{9/10} . \tag{132}$$

The equation that determines the radii at which $P_{rad} = P_{gas}$ also changes. Setting eq.(125) to unity we find

$$\frac{r}{J(r)^{16/21}} = 331 (\alpha M_8)^{2/21} (\dot{m}/\eta)^{16/21} [1 - f(r)]^{6/7} . \tag{133}$$

4.3 The f-parameter effects

To study the disc spectrum when $f \neq 0$ we consider following four cases:

- case 1: $f = 0$ throughout the disc, which is what we assumed in chapters 2 and 3,
- case 2: $f = 0.99$ for $r < r_2 = 4.68$ and $f = 0$ for the rest of the disc,
- case 3: $f = 0.99$ for $r < r_3 = 12.33$ and $f = 0$ for the rest of the disc,
- case 4: f is decreasing with increasing radius as: $f(r) = (\sqrt{r_{outer}} - \sqrt{r})/\sqrt{r_{outer}}$.

Cases 2 and 3 describe scenarios where 10% and 50% of the total accretion power is taken from the disc, respectively. This power may be used to power the X-ray source, or to launch outflows, assuming that X-rays are emitted close to the central BH, and the most powerful outflows originate from the inner disc. In case 4, f is close to unity in the inner disc and it approaches zero as we move on to the outer parts, meaning that more and more of the gravitational energy is given to the disc at large radii.

Figure (21) shows plots of $H/R, n, P_{rad}/P_{gas}, T, \tau_d, \tau_{eff}$ as a function of the radius, for the cases 1,2 and 3 and accretion rates $\dot{m} = 0.05, 0.5$. The layout of the panels in Fig.(21) is the same as in Fig.(14) of section 3.6, but we have replaced the disc pressure panel with a panel which shows the P_{rad}/P_{gas} ratio. After all, the behaviour of the pressure is very similar to that of the temperature.

At the top left panel, we present the height of the disc. For cases 2 and 3 the inner disc is very thin, and thus we notice high densities. At radii $r_2 = 4.68$, for case 2, and $r_3 = 12.33$, for case 3, the disc height suddenly increases and the density falls off. The reason for this discontinuity, is the assumed, abrupt change of f from 0.99 to 0. This change also affects pressure. As we can see from the middle left panel, when $f = 0.99$ we have a gas dominated zone, which shifts to a radiation zone as soon as f drops to zero. The temperature is shown in the middle right panel. The inner disc temperature in cases 2 and 3 is significantly larger than the temperature in case 1. In the bottom panels, we present the scattering and the effective optical depth. Both remain above unity, except for the case of $\dot{m} = 0.5$ in the bottom right panel. Cases 2 and 3 show larger values of τ_d and τ_{eff} at small radii in comparison with case 1. At radii larger than r_2 and r_3, the disc parameters are identical to these of case 1.

Figure (22) shows the disc parameters for the cases 1 and 4, for $\dot{m} = 0.05, 0.5$. We notice that the radiation zone disappears completely in case 4, for the smallest accretion rate, i.e. $\dot{m} = 0.05$.

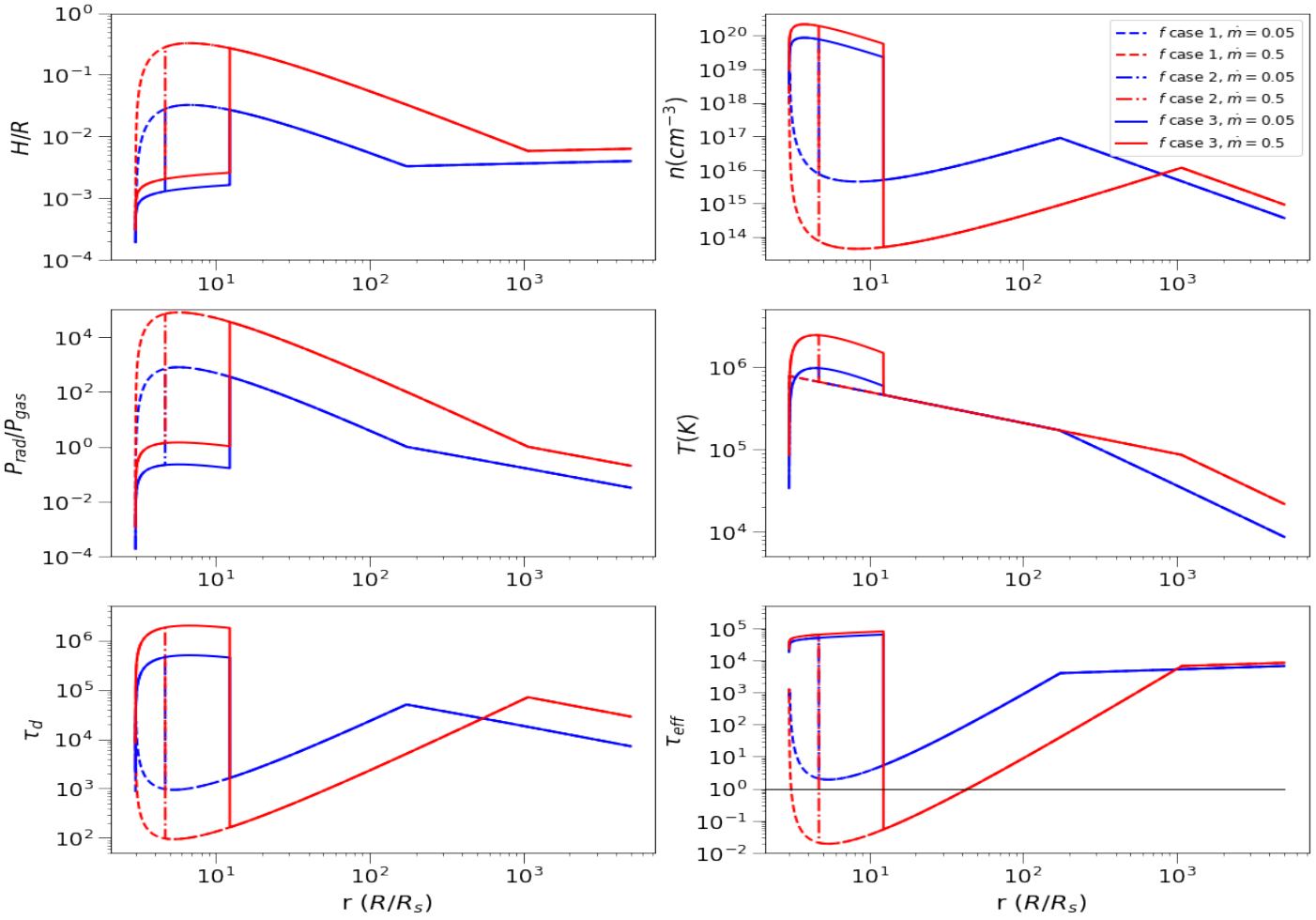

Figure 21: $H/R, n, P_{rad}/P_{gas}, T, \tau_d, \tau_{eff}$ for a BH of mass $M_8 = 0.1$ and accretion rates $\dot{m} = 0.05, 0.5$, for case 1: $f = 0$ at all r, case 2: $f = 0.99$ at $r < 4.68$, and case 3: $f = 0.99$ at $r < 12.33$.

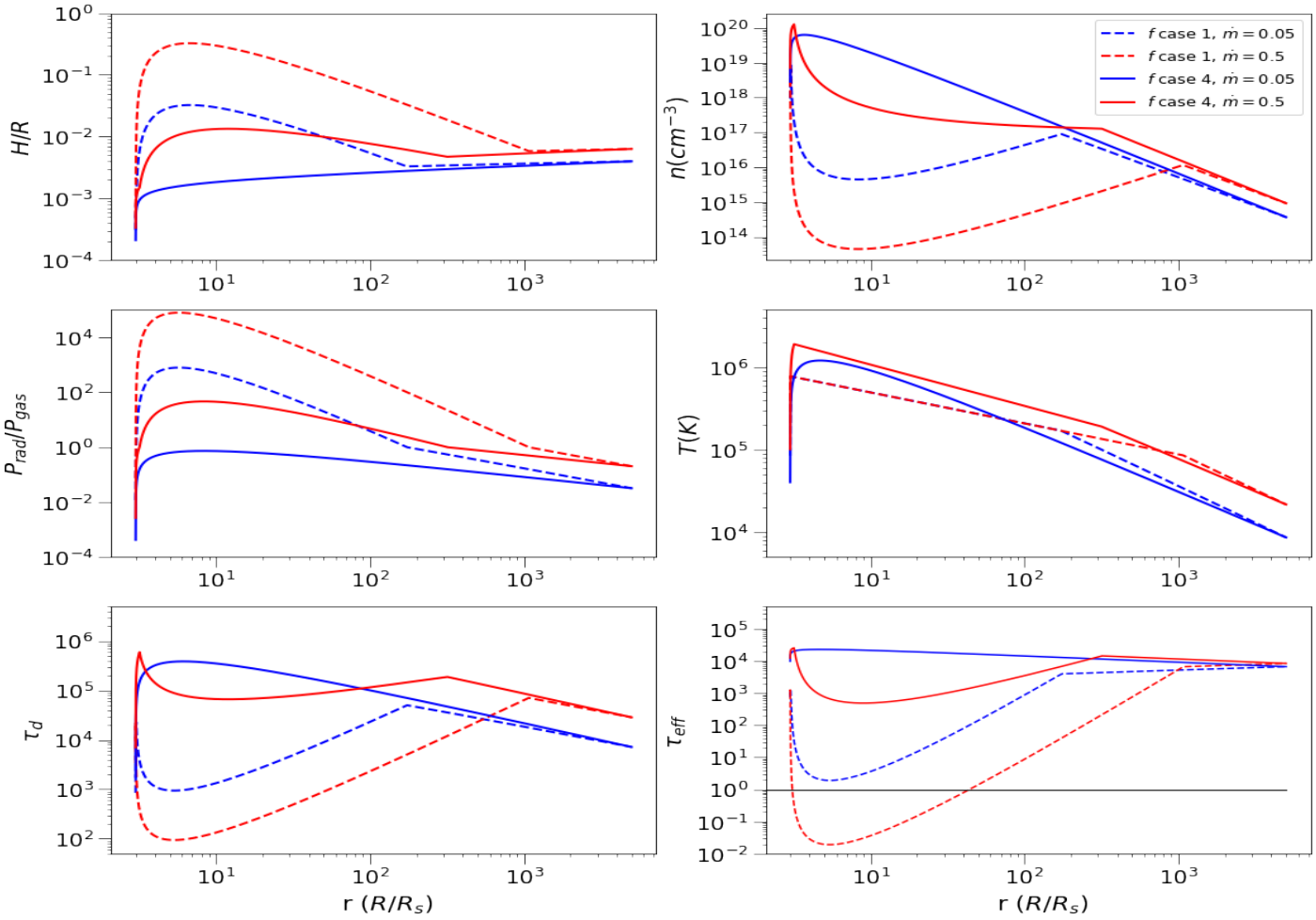

Figure 22: $H/R, n, P_{rad}/P_{gas}, T, \tau_d, \tau_{eff}$ for a BH of mass $M_8 = 0.1$ and accretion rates $\dot{m} = 0.05, 0.5$, for case 1: $f = 0$ at all r, and case 4: $f = (\sqrt{5000} - \sqrt{r})/\sqrt{5000}$.

Overall, in case 4 the disc height is smaller, and thus disc density, and temperature, as well as the scattering and effective optical depth are higher. In fact, the disc remains effectively optically thick, even when the radiation pressure dominates for $\dot{m} = 0.5$, as can be observed in the bottom right panel of Fig.(22).

4.3 The disc spectrum and the f parameter

Knowing how the disc equations change with the introduction of f, we can compute the disc energy spectrum using eq.(112), and following the same procedure as in section 3.7.2. As we explained in that section, we need to calculate $T_s(r)$ first. When $f = 0$, $T_s(r)$ is defined by eq.(54). But in the case when $f \neq 0$, this equation has to be modified accordingly, as follows

$$4\pi \frac{k^4 T_s^4(r)}{h^3 c^2} \int_0^\infty \frac{x^3 dx}{(e^x - 1)(1 + \sqrt{1 + \kappa_\tau/\kappa_{ff}})} = [1 - f(r)] \frac{m_p c^3}{\sigma_\tau R_s} \frac{3}{8} r^{-3} \dot{m} (1 - \sqrt{\frac{3}{r}}) \, . \tag{134}$$

We solved the equation above numerically, as described in section 3.7.1. Figure (23) shows the temperature radial profiles for the four cases of f considered so far. Since $T_s(r)$ depends on the amount of power that is available for the disc heating, case 1 (dashed blue line), where all the

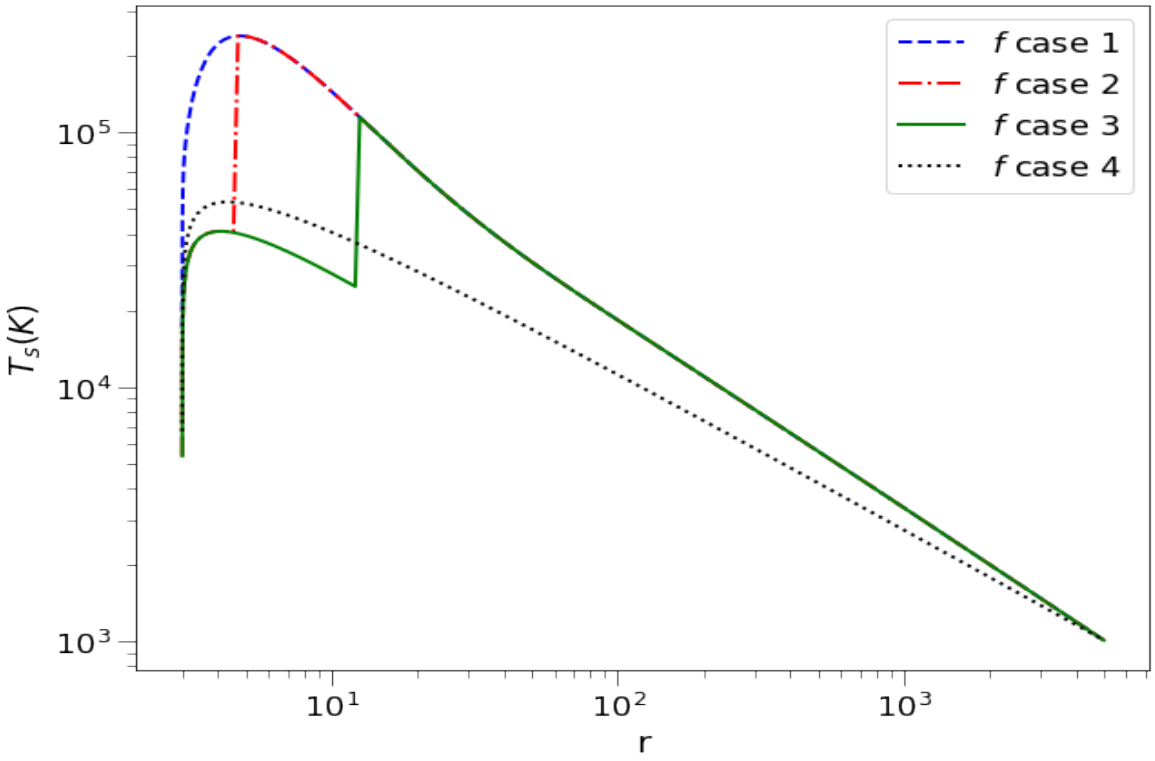

Figure 23: Surface temperature of accretion disc for a BH of mass $M_8 = 0.1$ and accretion rate $\dot{m} = 0.05$ for different cases of f.

gravitational power is radiated away, corresponds to the largest temperature. The dotdashed red and solid green lines, i.e. case 2 and 3, show the smallest temperatures at small radii where $f = 0.99$. As expected, when f drops to zero, they coincide with the blue line. In case 4 (black dotted line) the temperature remains relatively small throughout the disc, since power is taken away from the disc at all radii. At the outermost radius, all temperatures converge.

Having the surface temperature, we can calculate the disc spectrum. Figure (24) shows the resulting disc spectra, in the frequency range $10^{13} - 3 \times 10^{16} Hz$. The case 1 and 2 spectra, i.e. blue and red curves, are almost identical. We notice that the blue curve is slightly above the red one at high frequencies, due to the higher temperatures in case 1. Only a small part of the total gravitational power is taken away from the disc in case 2, and this effect cannot alter the spectrum considerably. On the other hand, the green spectrum has noticeably smaller values at high frequencies, since half of the gravitational power is taken away from the disc. The case 4 spectrum is significantly lower than the other cases, at all frequencies. Actually, the SED shape in the optical/UV band is significantly different in the last case as well (the slope of $F(\nu)$ between $\sim 10^{14}$Hz and $\sim 10^{15}$Hz is approximately $F(\nu) \propto \nu^{-1/3}$ in case 4).

Figure (25) shows the energy spectra in units of $\nu F(\nu)$ for the same cases of f. We notice, that the maximum emitted power decreases with increasing f, and the respective frequency of the peak power is shifted to smaller frequencies. This is because the spectrum at high frequencies is determined by the inner parts of the disc, which have high temperatures. As the gravitational energy released in those parts is not radiated away, these parts do not contribute to the disc energy spectrum. As a result, the peak of the spectrum shifts to smaller frequencies. The peaks of the cases 1, 2, 3, and 4 are located at $\nu_{peak,1} \approx 5.8 \times 10^{15}$Hz, $\nu_{peak,2} \approx 4.8 \times 10^{15}$Hz, $\nu_{peak,3} \approx 3.1 \times 10^{15}$Hz, and $\nu_{peak,4} \approx 2.2 \times 10^{15}$Hz respectively.

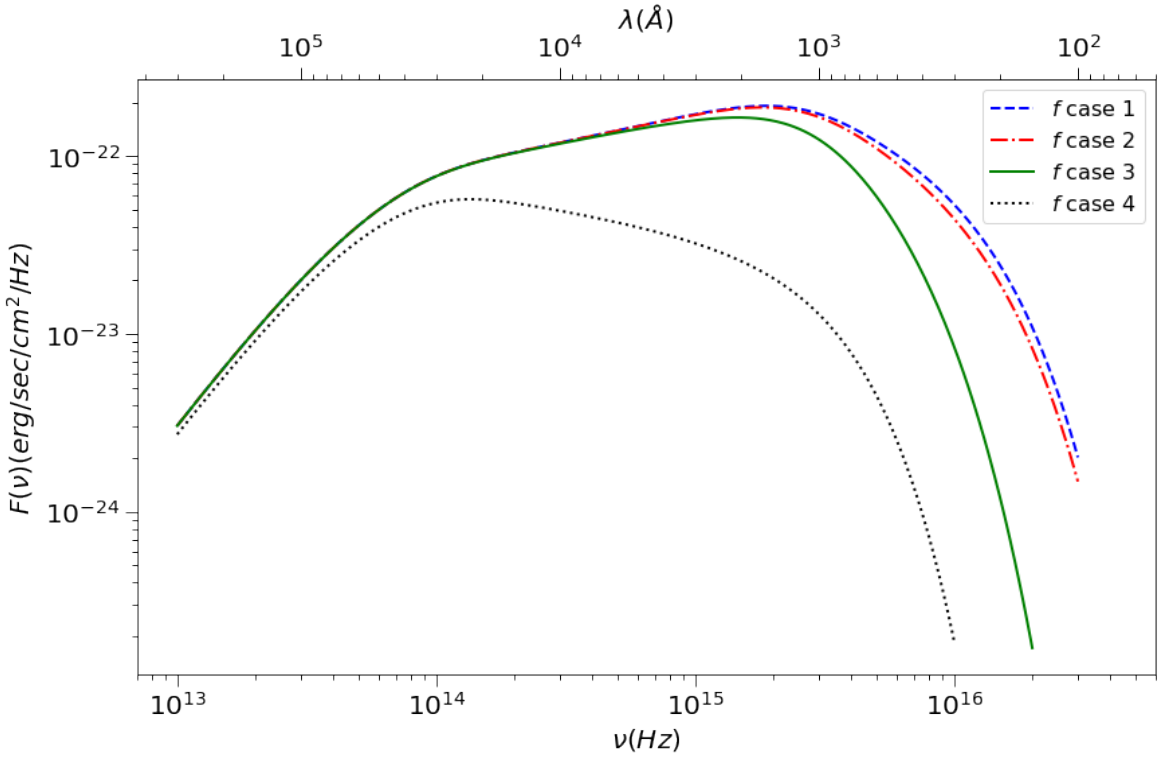

Figure 24: Disc spectra for a BH of mass $M_8 = 0.1$ and accretion rate $\dot{m} = 0.05$ for different cases of f.

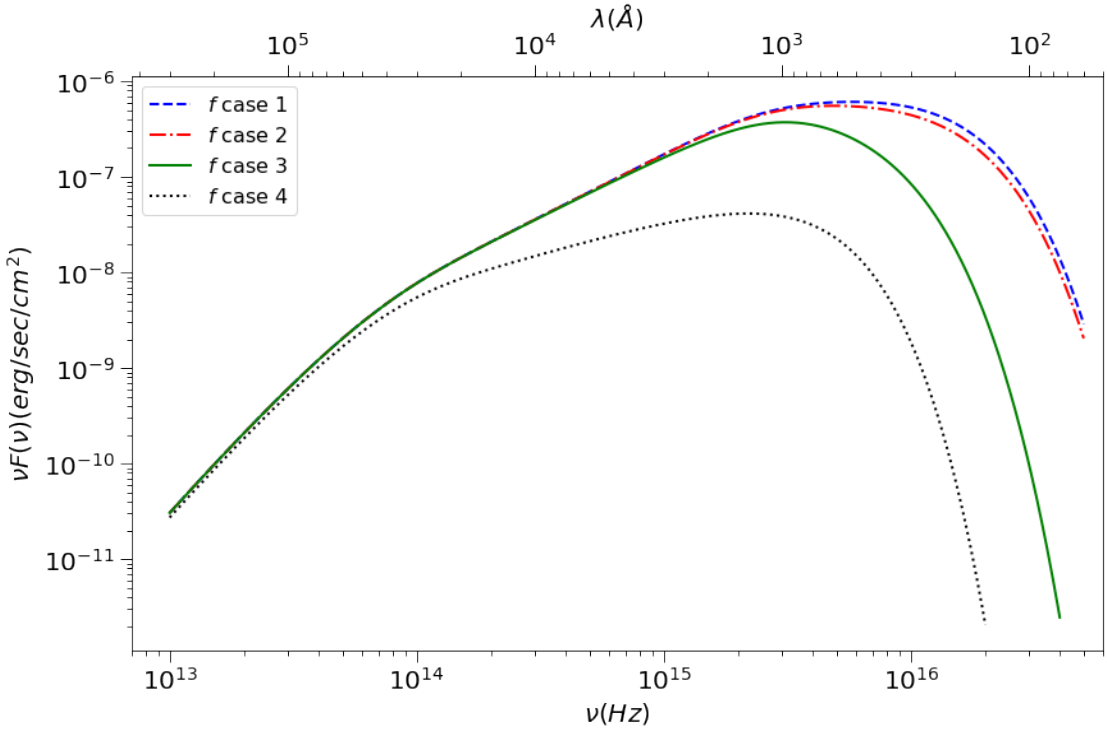

Figure 25: Same as in Fig.(24) but in $\nu F(\nu)$ units.

Chapter 5: Summary and conclusions

The main objective of this work was to study the energy spectrum of an accretion disc around SMBHs, beyond the simple assumption of black body emission. We considered the more realistic scenario where absorption and scattering effects take place, and we also examined how the spectrum changes when a percentage of the accretion power is taken from the disc and is (possibly) used to power the X-ray source and/or outflows.

We started by making standard assumptions for the disc rotation, and we used the conservation of mass and angular momentum for a disc annulus, to derive an expression for the gravitational power released, due to viscosity. Assuming the available accretion power is used to heat the disc, we studied its temperature profile and energy spectrum, by assuming that each disc annulus emits as a black body.

In chapter 3, we considered the more realistic case that free-free absorption and Thomson scattering take place in the disc, and thus the emission is that of a modified black body. To calculate the disc spectrum in this case, we need to compute the surface temperature and the density of the disc. To derive the latter we proceeded by solving the disc equations in the radiation pressure and gas pressure regimes, as was initially performed by Svensson & Zdziarski(1994). We investigated how the gas and radiation pressure parameters vary as a function of radius, for various accretion rates, and we determined the disc parameters accordingly. Then, we numerically computed the surface temperature by solving the energy balance equation for the "modified" emission. Using the resulting temperature we calculated the modified black body spectrum and checked how it compares with the simple black body case.

Lastly, we assumed that a fraction of the gravitational power, say f, is not dissipated to the disc, and could be given to the X-ray source, outflows, and winds. We then investigated how the introduction of f affects the disc parameters in the radiation and gas pressure regimes. Then, we computed the disc temperature profile and the energy spectrum assuming three different cases regarding the dependence of f on disc radius, and we compared the results.

Our findings from this work can be summarized as follows:

1. We provided equations that can be used to calculate the radius where the radiation and gas pressure become equal, for any black hole mass and accretion rate. We calculated $r_{eq,1}$ and $r_{eq,2}$ using eq.(96) and we plotted $r_{eq,2}$ as a function of $\dot{m}$ for all the BH masses we considered. We fitted a relation of the form

$$r_{eq,2}(\dot{m}, M_8) = A \times \left(\dot{m}/0.05\right)^s \tag{135}$$

to the $r_{eq,2}$ versus $\dot{m}$ data. The model fitted the data well with

$$A(M_8) = 45.69 \times log(M_8) + 215.02 \tag{136}$$

$$s(M_8) = -0.0106 \times log(M_8) + 0.8162\ . \tag{137}$$

Equations (135), (136) and (137) can be used to compute directly the radius where $P_{rad} = P_{gas}$, for any values of M_8 and $\dot{m}$ (in the range $[0.01, 10]$ and $[0.005, 0.5]$ respectively), without solving numerically eq.(96). We note that these equations provide $r_{eq,2}$. The inner radius where $P_{rad} = P_{gas}$ is close to r_{isco}, and thus one can safely assume that the inner disc is radiation pressure dominated. This assumption becomes more accurate for large values of $M_8, \dot{m}$.

2. We computed the disc surface temperature profile and the energy spectrum of the modified black body emission case and compared it with the black body case. The temperature in the

modified case is larger at the inner part of the disc, i.e. at $R < 100R_s$. The disc spectra when we assume black body and modified black body emission agree well below $\sim 10^{14}$Hz. At higher frequencies the two spectra differ by more than $\sim 1\%$. At frequencies higher than $\sim 10^{15}$Hz the difference is of the order of $\sim 10\%$, and increases with increasing frequency reaching $\sim 100\%$ in the far-UV. This happens because, in the case when we assume modified black body emission, the temperature is high in the inner disc. As a result, the emitted power at high frequencies is higher in this case. In addition, Thomson scattering dominates high-frequency emission, since free-free absorption falls off at high frequencies. Consequently, the intensity of modified black body emission is not well approximated by the Planck function which leads to noticeable differences between the two cases.

3. We computed the disc surface temperature profile and the modified disc spectrum when a fraction f of the accretion power is not dissipated to the disc, but it may be given to the X-ray source and outflows. Apart from the already studied case where $f = 0$ throughout the disc (case 1) we considered 3 new cases, i.e. case 2: $f = 0.99$ for $r < 4.68$ and $f = 0$ for the rest of the disc, case 3: $f = 0.99$ for $r < 12.33$ and $f = 0$ for the rest of the disc, and case 4: $f = (\sqrt{r_{outer}} - \sqrt{r})/\sqrt{r_{outer}}$. In all cases, we also assumed modified black body emission. Our results are as follows:

   (a) The disc temperature decreases at those disc regions where $f \neq 0$. Since we assumed that in these regions $f \approx 1$, the disc temperature decreases significantly.

   (b) The disc spectrum, in general, is affected at high frequencies, i.e. at frequencies higher than $\sim 10^{15}$Hz (or at wavelengths smaller than 4000Å), in cases 2 and 3. The emitted power decreases when $f \neq 0$, as expected. In case 3, where half of the accretion power released in the disc is taken away, the disc emission decreases exponentially below $\sim$ 1000Å.

   (c) The effects of f on the disc temperature and spectrum are even more significant in case 4. The disc temperature is smaller at all radii (when compared with the temperature in case 1). Consequently, the case 4 disc spectrum is significantly different when compared with the disc spectrum in all other cases, and not only because the emitted power starts decreasing exponentially at a lower frequency. In fact, this frequency is roughly similar in the case 3 and 4 spectra. The main effect in the case 4 disc spectrum is that the emitted power decreases at all wavelengths higher than $\sim$ 30000Å(in the near infrared part of the spectrum). The amount of power "lost" from the emitted disc spectrum increases with increasing frequency. As a result, it is the slope of the overall spectrum, both in $[\nu, F(\nu)]$ and in the $[\nu, \nu F(\nu)]$ representations that changes considerably.

   Most of the theoretical disc spectra that are used to fit experimental data do not take into account the possibility that f may not be zero. Our results show that such a possibility has significant effects to the expected disc spectrum, in the optical and UV bands, and it should be taken into consideration when fitting data.

Appendices

Appendix A: Solution of the disc equations

Here we derive the expressions (82)-(88) for the disc height, density, pressure, temperature, scattering optical depth, effective optical depth and the pressure ratio in the radiation domination regime. We solve eq.(77) for the density

$$P = \rho \frac{GM}{R^3} H^2 \Rightarrow \rho = \frac{P}{H^2} \frac{R^3}{GM} \, . \tag{138}$$

We can also get an expression for the temperature as follows

$$P = P_{rad} = \frac{4\sigma}{3c} T^4 \Rightarrow T^4 = \frac{3c}{4\sigma} P \, . \tag{139}$$

Next, we take eq.(80) and substitute the optical depth $\tau = \rho H \sigma_T / m_p$ and the temperature

$$\frac{4\sigma}{3\tau} T^4 = \frac{3}{8\pi} \frac{GM\dot{M}}{R^3} J(R) \Rightarrow \frac{cm_p}{\sigma_T} \frac{P}{\rho H} = \frac{3}{8\pi} \frac{GM\dot{M}}{R^3} J(R) \, , \tag{140}$$

where $J(R) = \left(1 - \sqrt{\frac{3R_s}{R}}\right)$. Then we substitute eq.(138) for the density into eq.(140). It turns out that the pressure cancels out and we get an expression with only the disc height as the unknown,

$$\frac{cm_p}{\sigma_T} H \frac{GM}{R^3} = \frac{3}{8\pi} \frac{GM\dot{M}}{R^3} J(R) \Rightarrow H = \frac{3}{8\pi} \frac{\sigma_T}{cm_p} \dot{M} J(R) \, . \tag{141}$$

Then we substitute the density into eq.(78) and solve for the pressure

$$H^2 \sqrt{P\rho} = \frac{\dot{M}}{3\pi\alpha} J(R) \Rightarrow H^2 \sqrt{\frac{P^2}{H^2} \frac{R^3}{GM}} = \frac{\dot{M}}{3\pi\alpha} J(R) \Rightarrow$$

$$P = \frac{\dot{M}}{3\pi\alpha} \sqrt{\frac{GM}{R^3}} \frac{1}{H} J(R) \, . \tag{142}$$

We use the expression for H we just derived to find the pressure

$$P = \frac{8}{9} \frac{cm_p}{\sigma_T} \alpha^{-1} \sqrt{\frac{GM}{R^3}} \, . \tag{143}$$

We can now find the density from eq.(138)

$$\rho = \frac{512\pi^2}{81} (\frac{cm_p}{\sigma_T})^3 \alpha^{-1} \dot{M}^{-2} J(R)^{-2} \sqrt{\frac{R^3}{GM}} \, . \tag{144}$$

Then we find the temperature from eq.(139)

$$T = \left(\frac{2}{3} \frac{c^2 m_p}{\sigma \sigma_T} \alpha^{-1} \sqrt{\frac{GM}{R^3}}\right)^{1/4} \tag{145}$$

Next, we solve for the optical depth

$$\tau = \frac{64\pi}{27} \frac{c^2 m_p}{\sigma_T} \alpha^{-1} \dot{M}^{-1} J(R)^{-1} \sqrt{\frac{R^3}{GM}} \, . \tag{146}$$

The effective optical depth is given by

$$\tau_{eff} = \sqrt{\kappa_{ff}\rho H\tau} \Rightarrow \tau_{eff} = 180.4(\frac{m_p^{41}c^{42}}{\sigma_T^{41}\sigma^{-7}})^{1/16}\alpha^{-17/16}[\dot{M}J(R)]^{-2}(\frac{R^3}{GM})^{31/32} . \quad (147)$$

To find the pressure ratio we need the gas pressure

$$P_{gas} = \frac{2\rho kT}{m_p} \Rightarrow P_{gas} = \frac{1024\pi^2}{81}(\frac{2}{3})^{1/4}k(\frac{c^{14}m_p^9}{\sigma\sigma_T^{13}})^{1/4}\alpha^{-5/4}[\dot{M}J(R)]^{-2}(\frac{R^3}{GM})^{3/8} . \quad (148)$$

Then the pressure ratio is

$$\frac{P_{rad}}{P_{gas}} = \frac{9}{128\pi^2}(\frac{3}{2})^{1/4}(\frac{\sigma\sigma_T^9}{c^{10}m_p^5})^{1/4}\alpha^{1/4}[\dot{M}J(R)]^2(\frac{R^3}{GM})^{-7/8} . \quad (149)$$

To get these expressions to the form of (82)-(88) we need to introduce the dimensionless variables of section 2.7.1, .i.e.

$$r \equiv \frac{R}{R_s},\ \dot{m} \equiv \frac{\eta\dot{M}c^2}{L_{Edd}} , \quad (150)$$

with

$$L_{Edd} = 2\pi\frac{m_pc^3}{\sigma_T}R_s , \quad (151)$$

and $R_s = 2GM/c^2$. Equation (141) becomes

$$\frac{H}{R} = \frac{3}{8\pi}\frac{\sigma_T}{cm_p}\dot{M}\frac{1}{R}J(R) \Rightarrow \frac{H}{R} = \frac{3}{8\pi}\frac{\sigma_T}{cm_p}\frac{L_{edd}\dot{m}}{\eta c^2}\frac{1}{rR_s}J(r) \Rightarrow$$

$$\frac{H}{R} = \frac{3}{8\pi}\frac{\sigma_T}{cm_p}2\pi\frac{m_pc^3}{\sigma_T}R_s\frac{1}{R_sc^2}\frac{\dot{m}}{\eta}\frac{1}{r}J(r) \Rightarrow \frac{H}{R} = \frac{3}{4}r^{-1}\frac{\dot{m}}{\eta}J(r) , \quad (152)$$

which is eq.(82). Note that

$$J(R) = \left(1-\sqrt{\frac{3R_s}{R}}\right) = \left(1-\sqrt{\frac{3R_s}{rR_s}}\right) = \left(1-\sqrt{\frac{3}{r}}\right) = J(r) . \quad (153)$$

Let us also perform the substitutions for the density

$$\rho = \frac{512\pi^2}{81}(\frac{cm_p}{\sigma_T})^3\alpha^{-1}(\frac{\dot{m}}{c^2\eta}2\pi\frac{m_pc^3}{\sigma_T}R_s)^{-2}\sqrt{\frac{r^3R_s^3}{c^2R_s/2}}J(r)^{-2} \Rightarrow$$

$$\rho = \frac{512\pi^2}{81}(2\pi)^{-2}\sqrt{2}\frac{c^3m_p^3m_p^{-2}c^{-2}R_s^{-2}R_s}{\sigma_T\sigma_T^{-2}c}\alpha^{-1}[\frac{\dot{m}}{\eta}J(r)]^{-2}$$

$$\rho = \frac{128\sqrt{2}}{81}\frac{m_p}{\sigma_TR_s}\alpha^{-1}r^{3/2}[\frac{\dot{m}}{\eta}J(r)]^{-2} . \quad (154)$$

Then we can substitute $m_p = 1.6726\times10^{-24}g$, $\sigma_T = 6.652\times10^{-25}cm^2$ and

$$R_s = \frac{2GM}{c^2} = \frac{2G}{c^2}\frac{M}{10^8M_\odot}10^8M_\odot = 2.95\times10^{13}M_8 , \quad (155)$$

where $G = 6.6743\times10^{-8}cm^3g^{-1}s$, $c = 2.998\times10^{10}cm/s$, $M_\odot = 1.989\times10^{33}g$ and $M_8 = M/(10^8M_\odot)$ to find

$$\rho = 1.9\times10^{-13}(\alpha M_8)^{-1}r^{3/2}[(\dot{m}/\eta)J(r)]^{-2}\ (\mathrm{g\ cm^{-3}}) . \quad (156)$$

The rest of the expressions for $P, T, \tau, \tau_{eff}, P_{rad}/P_{gas}$ can be found similarly.

References

[1] Carroll B. W., Ostlie D. A, 2007, "An Introduction to Modern Astrophysics", 2nd ed., Pearson Addison-Wesley

[2] Czerny B. & Naddaf M. H., 2019, "Accretion in Active Galactic Nuclei", PoS

[3] Dominik C., 2015, "Disk formation and structure", EPJ Web of Conferences, Vol.102, 00002

[4] Frank J, King A., Raine D., 1992, "Accretion Power in Astrophysics", 2nd ed., Cambridge University Press

[5] Pariev V. I., Blackman E. G. & Boldyrev S. A., 2003, "Extending the Shakura-Sunyaev approach to a strongly magnetized accretion disc model", A&A, Vol.407, p.403

[6] Peterson B. M, 1997, "An Introduction to Active Galactic Nuclei", Cambridge University Press

[7] Pringle J. E., 1981, "Accretion Discs in Astrophysics", ARA&A, Vol.19, p.137

[8] Rybicki, G. B., & Lightman, A. P. 1979, "Radiative Processes in Astrophysics", New York: John Wiley

[9] Sadowski A., Lasota J. P., Abramowicz M. A. & Narayan R., 2016, "Energy flows in thick accretion discs and their consequences for black hole feedback", MNRAS, Vol.456, p.3915 Pringle J. E., 1981, "Accretion Discs in Astrophysics", ARA&A, Vol.19, p.137

[10] Shakura, N. I. & Sunyaev, R. A., 1973, "Black holes in binary systems. Observational appearance", A&A, Vol.24, p.337

[11] Svensson, R. & Zdziarski, A. A., 1994, "Black hole accretion disks with coronae", ApJ, Vol.436, p.599

[12] Zimmerman E. R., Narayan R., McClintock J. E. & Miller J. M., 2004, "Multi-Temperature Blackbody Spectra of Thin Accretion Disks With and Without a Zero-Torque Inner Boundary Condition", ApJ, Vol.618, p.832